PREPARATION AND OPERATIONS OF THE MISSION PERFORMANCE CENTRE (MPC) FOR THE COPERNICUS SENTINEL-3 MISSION

S3-A OLCI Cyclic Performance Report

Cycle No. 022

Start date: 03/09/2017

End date: 30/09/2017

SENTINEL 3

Mission Performance Centre

Ref.: S3MPC.ACR.PR.01-022
Issue: 1.0
Date: 06/10/2017
Contract: 4000111836/14/I-LG

Customer:	ESA	**Document Ref.:**	S3MPC.ACR.PR.01-022
Contract No.:	4000111836/14/I-LG	**Date:**	06/10/2017
		Issue:	1.0

Project:	PREPARATION AND OPERATIONS OF THE MISSION PERFORMANCE CENTRE (MPC) FOR THE COPERNICUS SENTINEL-3 MISSION		
Title:	S3-A OLCI Cyclic Performance Report		
Author(s):	OLCI ESLs		
Approved by:	L. Bourg, OLCI ESL Coordinator	**Authorized by**	Frédéric Rouffi, OPT Technical Performance Manager
Distribution:	ESA, EUMETSAT, S3MPC consortium		
Accepted by ESA	S. Dransfeld, MPC Deputy TO for OPT P. Féménias, MPC TO		
Filename	S3MPC.ACR.PR.01-022 - i1r0 - OLCI Cyclic Report 022.docx		

Disclaimer

The work performed in the frame of this contract is carried out with funding by the European Union. The views expressed herein can in no way be taken to reflect the official opinion of either the European Union or the European Space Agency.

Changes Log

Version	Date	Changes
1.0	05/10/2017	First Version

List of Changes

Version	Section	Answers to RID	Changes

Table of content

TABLE OF CONTENT ..... **IV**

LIST OF FIGURES ..... **V**

1 INSTRUMENT MONITORING **1**

1.1 CCD TEMPERATURES 1
1.2 RADIOMETRIC CALIBRATION 2
1.2.1 Dark Offsets [OLCI-L1B-CV-230] *4*
1.2.2 Instrument response and degradation modelling [OLCI-L1B-CV-250] *8*
1.2.3 Ageing of nominal diffuser [OLCI-L1B-CV-240] *16*
1.2.4 Updating of calibration ADF [OLCI-L1B-CV-260] *16*
1.2.5 Radiometric Calibrations for sun azimuth angle dependency and Yaw Manoeuvres for Solar Diffuser on-orbit re-characterization [OLCI-L1B-CV-270 and OLCI-L1B-CV-280] *17*
1.3 SPECTRAL CALIBRATION [OLCI-L1B-CV-400] 17
1.4 SIGNAL TO NOISE ASSESSMENT [OLCI-L1B-CV-620] 17
1.4.1 SNR from Radiometric calibration data *17*
1.4.2 SNR from EO data *20*
1.5 GEOMETRIC CALIBRATION/VALIDATION 20

2 OLCI LEVEL 1 PRODUCT VALIDATION **24**

2.1 [OLCI-L1B-CV-300], [OLCI-L1B-CV-310] – RADIOMETRIC VALIDATION 24
2.1.1 S3ETRAC Service *24*
2.1.2 Radiometric validation with DIMITRI *25*
2.1.3 Radiometric validation with OSCAR *30*
2.2 [OLCI-L1B-CV-320] – RADIOMETRIC VALIDATION WITH LEVEL 3 PRODUCTS 31

3 LEVEL 2 LAND PRODUCTS VALIDATION **32**

3.1 [OLCI-L2LRF-CV-300] 32
3.2 [OLCI-L2LRF-CV-410 & OLCI-L2LRF-CV-420] – CLOUD MASKING & SURFACE CLASSIFICATION FOR LAND PRODUCTS 32
3.3 VALIDATION OF INTEGRATED WATER VAPOUR OVER LAND 32

4 LEVEL 2 WATER PRODUCTS VALIDATION **33**

4.1 [OLCI-L2-CV-210, OLCI-L2-CV-220] – VICARIOUS CALIBRATION OF THE NIR AND VIS BANDS 33
4.2 [OLCI-L2WLR-CV-300, OLCI-L2WLR-CV-310, OLCI-L2WLR-CV-32, OLCI-L2WLR-CV-330, OLCI-L2WLR-CV-340, OLCI-L2WLR-CV-350, OLCI-L2WLR-CV-360 AND OLCI-L2WLR-CV-370] – LEVEL 2 WATER-LEAVING REFLECTANCE PRODUCT VALIDATION 33
4.3 [OLCI-L2WLR-CV530] VALIDATION OF AEROSOL PRODUCT 37
4.4 [OLCI-L2WLR-CV-380] DEVELOPMENT OF CALIBRATION, PRODUCT AND SCIENCE ALGORITHMS 38
4.4.1 Smile Correction at 681.25 nm (Oa10) *38*
4.4.2 Validity of the ANNOT_MIXR1 flag *42*

5 LEVEL 2 SYN PRODUCTS VALIDATION **46**

5.1 [SYN-L2-CV-100] 46

6 EVENTS **47**

7 APPENDIX A **48**

List of Figures

Figure 1: long term monitoring of CCD temperatures using minimum value (top), time averaged values (middle), and maximum value (bottom) provided in the annotations of the Radiometric Calibration Level 1 products, for the Shutter frames, all radiometric calibrations so far. ---------- 1

Figure 2: Same as Figure 1 for diffuser frames. ---------- 2

Figure 3: Sun azimuth angles during acquired Radiometric Calibrations (diffuser frame) on top of nominal yearly cycle (black curve). Diffuser 1 with diamonds, diffuser 2 with crosses, 2016 acquisitions in blue, 2017 in red. ---------- 3

Figure 4: Sun geometry during radiometric Calibrations on top of characterization ones (diffuser frame) 3

Figure 5: Dark Offset table for band Oa06 with (red) and without (black) HEP filtering (Radiometric Calibration of 22 July 2017). The strong HEP event near pixel 400 has been detected and removed by the HEP filtering. ---------- 4

Figure 6: Dark Offset for band Oa1 (top) and Oa21 (bottom), all radiometric calibrations so far except the first one (orbit 183) for which the instrument was not thermally stable yet. ---------- 5

Figure 7: map of periodic noise for the 5 cameras, for band Oa21. X-axis is detector number (East part, from 540 to 740, where the periodic noise occurs), Y-axis is the orbit number. The counts have been corrected from the west detectors mean value (not affected by periodic noise) in order to remove mean level gaps and consequently to have a better visualisation of the long term evolution of the periodic noise structure. Periodic noise amplitude is high in camera 2, 3 and 4. It is lower in camera 4 and small in camera 1. ---------- 6

Figure 8: Dark Current for band Oa1 (top) and Oa21 (bottom), all radiometric calibrations so far except the first one (orbit 183) for which the instrument was not thermally stable yet. ---------- 7

Figure 9: left column: ACT mean on 400 first detectors of Dark Current coefficients for spectral band Oa01 (top) and Oa21 (bottom). Right column: same as left column but for Standard deviation instead of mean. We see an increase of the DC level as a function of time especially for band Oa21. A possible explanation could be the increase of the number of hot pixels which is more important in Oa21 because this band is made of more CCD lines than band Oa01 and thus receives more cosmic rays impacts. It is known that cosmic rays degrade the structure of the CCD, generating more and more hot pixels at long term scales. ---------- 7

Figure 10: Gain Coefficients for band Oa1 (top) and Oa21 (bottom), all diffuser 1 radiometric calibrations so far except the first one (orbit 183) for which the instrument was not thermally stable yet. ---------- 8

Figure 11: camera averaged gain relative evolution with respect to “best geometry” calibration (22/11), as a function of elapsed time since launch; one curve for each band (see colour code on plots), one plot for each module. The star tracker anomaly fix (6/04/16) is represented by a vertical red dashed line. ---- 9

Figure 12: Camera-averaged instrument evolution since channel programming change (25/04/2016) and up to most recent calibration (22/09/2017) versus wavelength. ----------10

Figure 13: RMS performance of the Gain Model of current Processing Baseline as a function of orbit.---11

Figure 14: For the 5 cameras: Evolution model performance, as camera-average and standard deviation of ratio of Model over Data vs. wavelength, for each orbit of the test dataset, including 16 calibration in extrapolation, with a colour code for each calibration from blue (oldest) to red (most recent).----------12

Figure 15: model performance: ratio of model over data for all pixels (x axis) of all orbits (y axis), for channel Oa4. The outlying orbit #40 is that of 31/03/2017. ----------12

Figure 16: Evolution model performance, as ratio of Model over Data vs. pixels, all cameras side by side, over the whole current calibration dataset (since instrument programing update), including 16 calibration in extrapolation, channels Oa1 to Oa6. ----------13

Figure 17: same as Figure 14 for channels Oa7 to Oa14. ----------14

Figure 18: same as Figure 16 for channels Oa15 to Oa21.----------15

Figure 19: Signal to Noise ratio as a function of the spectral band for the 5 cameras. These results have been computed from radiometric calibration data. All calibrations except first one (orbit 183) are presents with the colours corresponding to the orbit number (see legend). The SNR is very stable with time: the curves for all orbits are almost superimposed. The dashed curve is the ESA requirement. -----18

Figure 20: long-term stability of the SNR estimates from Calibration data, example of channel Oa1.-----19

Figure 21: histograms of geolocation errors for the along-track (left) and across-track (right) directions, examples of 02/09/2017 (top) and 20/09/2017 (bottom).----------21

Figure 22: georeferencing error in along-track (left) and across-track (right) directions for all the GCPs, examples of 02/09/2017 (top) and 20/09/2017 (bottom).----------22

Figure 23: time series of geolocation errors for the along-track (blue) and across-track (red) directions over 15.6 months. ----------23

Figure 24: summary of S3ETRAC products generation for OLCI (number of OLCI L1 products Ingested, yellow – number of S3ETRAC extracted products generated, blue – number of S3ETRAC runs without generation of output product (data not meeting selection requirements), green – number of runs ending in error, red, one plot per site type). ----------25

Figure 25: Time-series of the elementary ratios (observed/simulated) signal from S3A/OLCI for (top to bottom) bands Oa03, Oa8 and Oa17 respectively over Six PICS Cal/Val sites. Dashed-green and orange lines indicate the 2% and 5% respectively. Error bars indicate the desert methodology uncertainty.-----27

Figure 26: The estimated gain values for S3A/OLCI over the 6 PICS sites identified by CEOS over the period April 2016 – July 2017 as a function of wavelength. Dashed-green and orange lines indicate the 2% and 5% respectively. Error bars indicate the desert methodology uncertainty. ----------27

Figure 27: Time-series of the elementary ratios (observed/simulated) signal from (black) S2A/MSI, (blue) S3A/OLCI for band Oa17 (865nm) over LIBYA1 and LIBYA4 sites. Dashed-green and orange lines indicate the 2% and 5% respectively. Error bars indicate the desert methodology uncertainty. ----------28

Figure 28: The estimated gain values (observed-signal /simulated-signal) averaged over different period from different sensors over PICS as function of wavelength.----------29

Figure 29: The estimated gain values for S3A/OLCI over the 6 Ocean CalVal sites (Atl-NW_Optimum, Atl-SW_Optimum, Pac-NE_Optimum, Pac-NW_Optimum, SPG_Optimum and SIO_Optimum) over the period December 2016 – September 2017 as a function of wavelength. Dashed-green, and orange lines indicate the 2%, 5% respectively. Error bars indicate the methodology uncertainty. ----------29

Figure 30: The estimated gain values for S3A/OLCI from Glint, Rayleigh and PICS over the period April 2016 – September 2017 for PICS and December 2016-September 2017 for Rayleigh and Glint methods as a function of wavelength. We use the gain value of Oa8 from PICS method as reference gain for Glint. Dashed-green and orange lines indicate the 2% and 5% respectively. Error bars indicate the methods uncertainties. ----------30

Figure 31: OSCAR Rayleigh results for July and Agust 2017. ----------31

Figure 32: Scatter plots of OLCI versus in situ radiometry (FR data) ----------34

Figure 33: Scatter plots of OLCI versus in situ radiometry (RR data)----------35

Figure 34: OLCI and AERONET-OC radiometric time on Gloria station. ----------37

Figure 35: The two extremes of the spectral response function of OLCI A bands ----------38

Figure 36: Simulated water leaving radiances for different amounts of Chlorophyll A. Overlaid are the relative spectral response function (and their spread)----------40

Figure 37: Chlorophyll A absorption and emission (in arb. units)----------41

Figure 38: Effect of spectral shift on water leaving reflectance. The dots are the nominal positions of the OLCI Bands 8,9,10 and 11----------41

Figure 39: Residual effect of spectral shift on water leaving reflectance after shift correction. The dots are the nominal positions of the OLCI Bands 8,9 and 10.----------42

Figure 40 : Oa01 water-leaving reflectance, clouds+cloud ambiguous+cloud margins in red, MIXR1 in blue. MIXR1 is raised because of small AOT in the absence of clouds.----------43

Figure 41 : Oa01 water-leaving reflectance, clouds+cloud ambiguous+cloud margins in red, MIXR1 in blue. MIXR1 is raised because of undetected small clouds.----------43

Figure 42 : Frequency of occurrence of raised MIXR1 flags as a function of aerosol optical thickness at 865 nm.----------44

Figure 43 : Oa01 water-leaving reflectance, clouds+cloud ambiguous+cloud margins in yellow, MIXR1 combined to AOT<0.05 in red, MIXR1 combined to AOT>0.05 in violet. ----------45

1 Instrument monitoring

1.1 CCD temperatures

The monitoring of the CCD temperatures is based on MPMF data extractions not yet operational. In the meantime, we monitor the CCD temperatures on the long-term using Radiometric Calibration Annotations (see Figure 1). Variations are very small (0.09 C peak-to-peak) and no trend can be identified. Data from current cycle (rightmost data points) do not show any specificity.

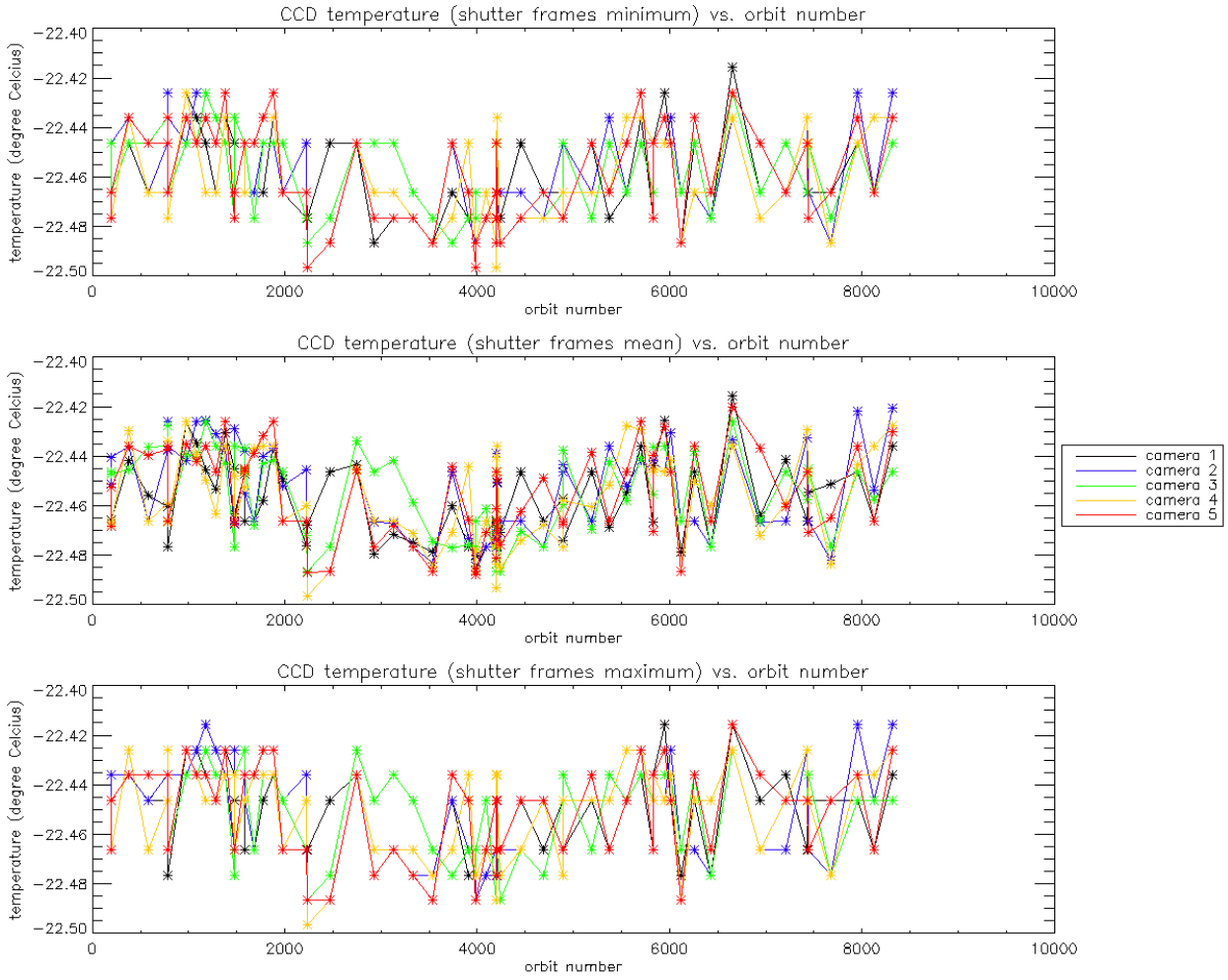

Figure 1: long term monitoring of CCD temperatures using minimum value (top), time averaged values (middle), and maximum value (bottom) provided in the annotations of the Radiometric Calibration Level 1 products, for the Shutter frames, all radiometric calibrations so far.

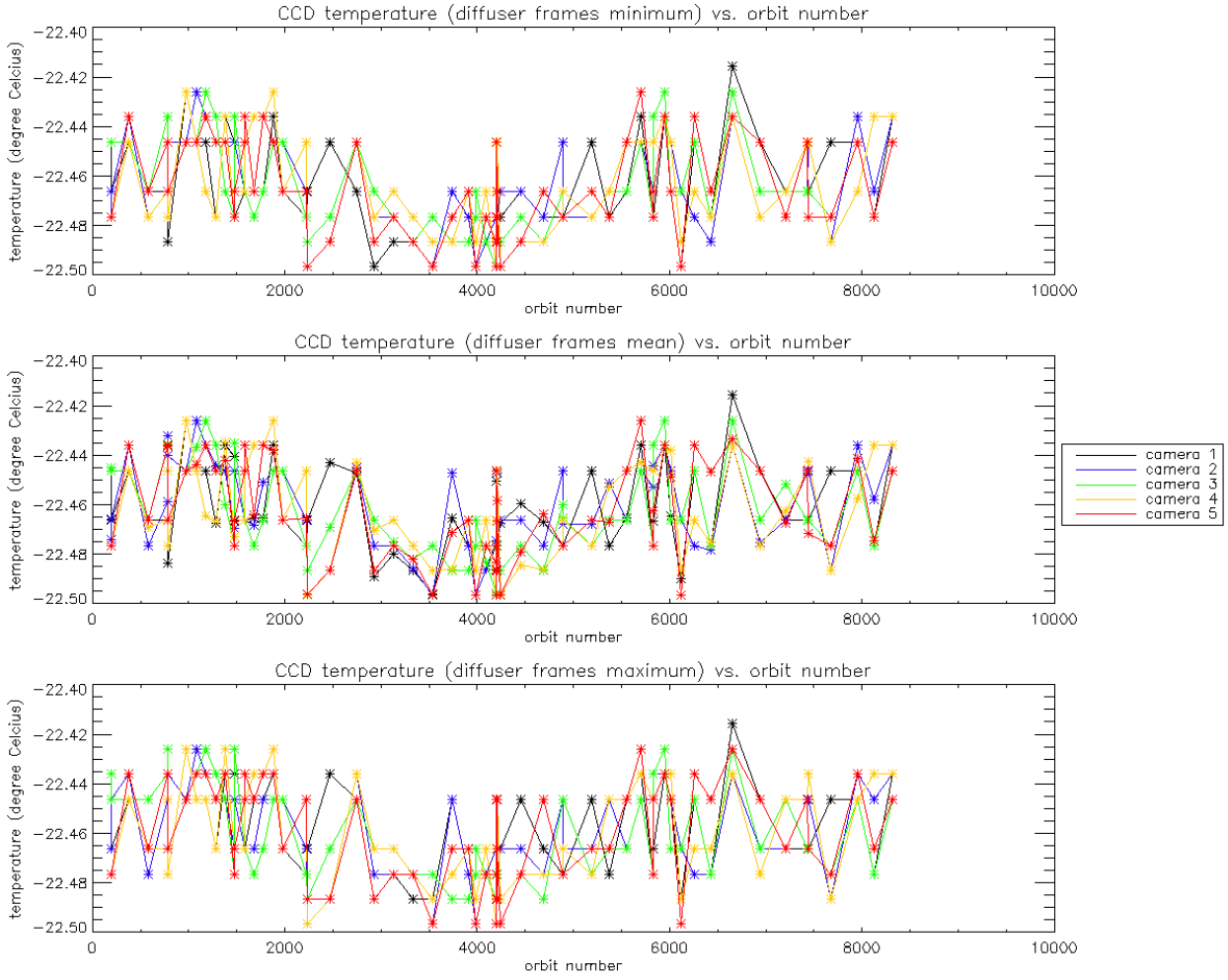

Figure 2: Same as Figure 1 for diffuser frames.

1.2 Radiometric Calibration

Two OLCI Radiometric Calibration Sequences have been acquired during Cycle 022:

- S01 sequence (diffuser 1) on 08/09/2017 17:34 to 17:36 (absolute orbit 8127)
- S01 sequence (diffuser 1) on 22/09/2017 01:24 to 01:25 (absolute orbit 8317)

The acquired Sun azimuth angles are presented on below, on top of the nominal values without Yaw Manoeuvre (i.e. with nominal Yaw Steering control of the satellite).

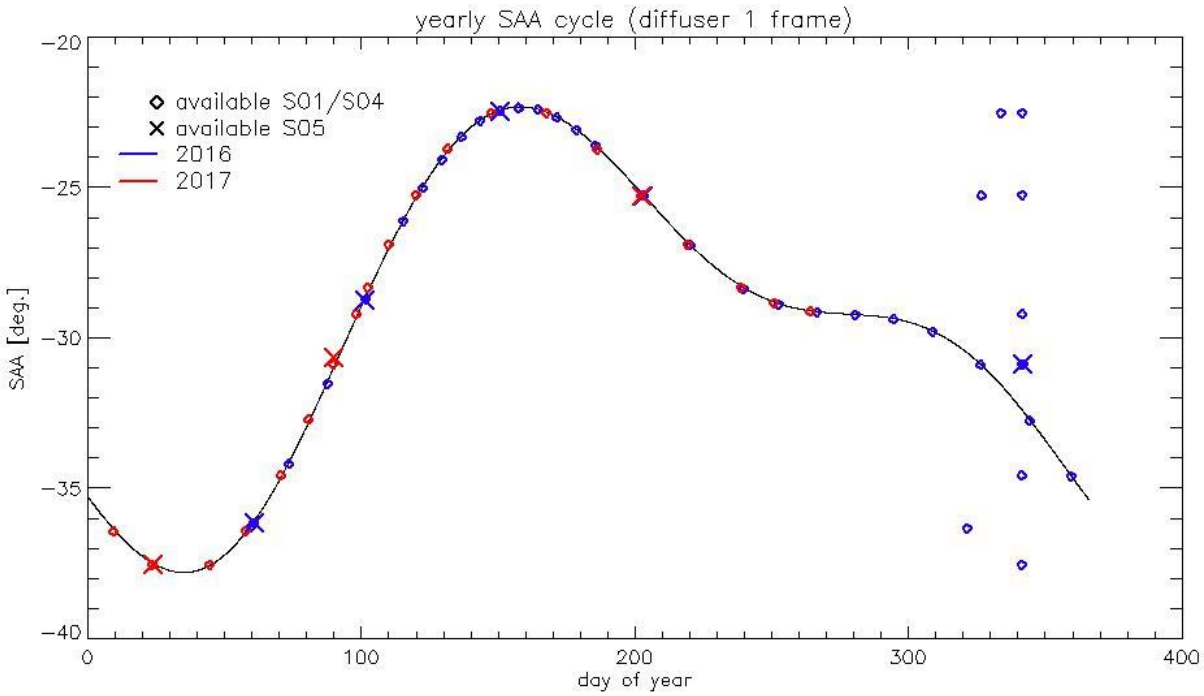

Figure 3: Sun azimuth angles during acquired Radiometric Calibrations (diffuser frame) on top of nominal yearly cycle (black curve). Diffuser 1 with diamonds, diffuser 2 with crosses, 2016 acquisitions in blue, 2017 in red.

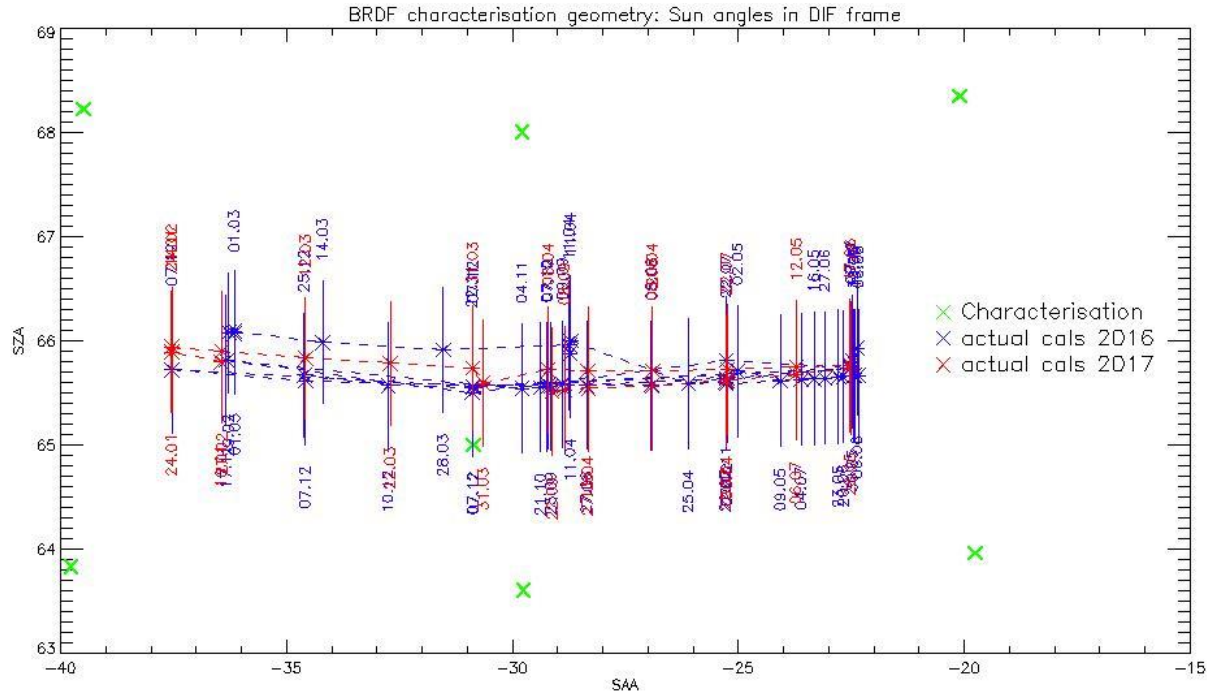

Figure 4: Sun geometry during radiometric Calibrations on top of characterization ones (diffuser frame)

This section presents the overall monitoring of the parameters derived from radiometric calibration data and highlights, if present, specificity of current cycle data.

1.2.1 Dark Offsets [OLCI-L1B-CV-230]

Note about the High Energy Particles:

The filtering of High Energy Particle (HEP) events from radiometric calibration data has been implemented (for shutter frames only) in a post processor, allowing generating Dark Offset and Dark Current tables computed on filtered data. The post-processor starts from IPF intermediate data (corrected counts), applies the HEP detection and filtering and finally computes the Dark Offset and Dark Current tables the same way as IPF. An example of the impact of HEP filtering is given in Figure 5.

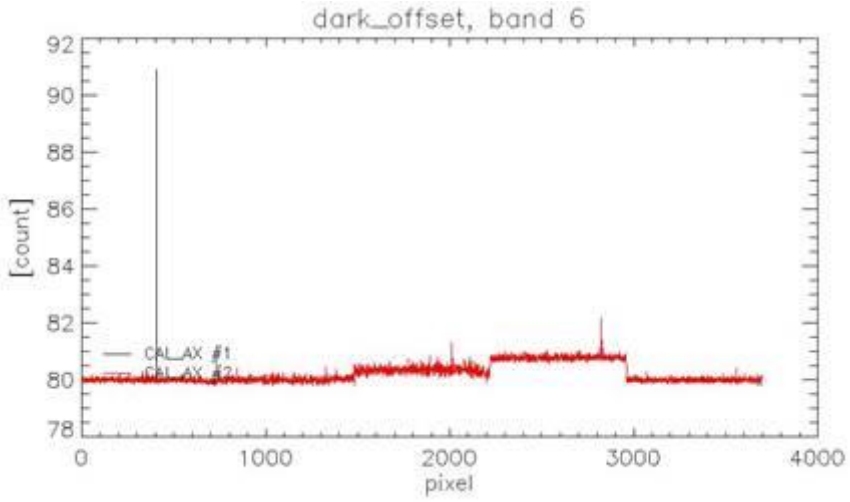

Figure 5: Dark Offset table for band Oa06 with (red) and without (black) HEP filtering (Radiometric Calibration of 22 July 2017). The strong HEP event near pixel 400 has been detected and removed by the HEP filtering.

All results presented below in this section have been obtained using the HEP filtered Dark Offset and Dark Current tables.

Dark offsets

Dark offsets are continuously affected by the global offset induced by the Periodic Noise on the OCL convergence. Current Cycle calibrations are affected the same way as others. The amplitude of the shift varies with band and camera from virtually nothing (e.g. camera 2, band 0a1) to up to 5 counts (Oa21, camera 3). The Periodic Noise itself comes on top of the global shift with its known signature: high frequency oscillations with a rapid damp. This effect remains more or less stable with time in terms of amplitude, frequency and decay length, but its phase varies with time, introducing the global offset mentioned above.

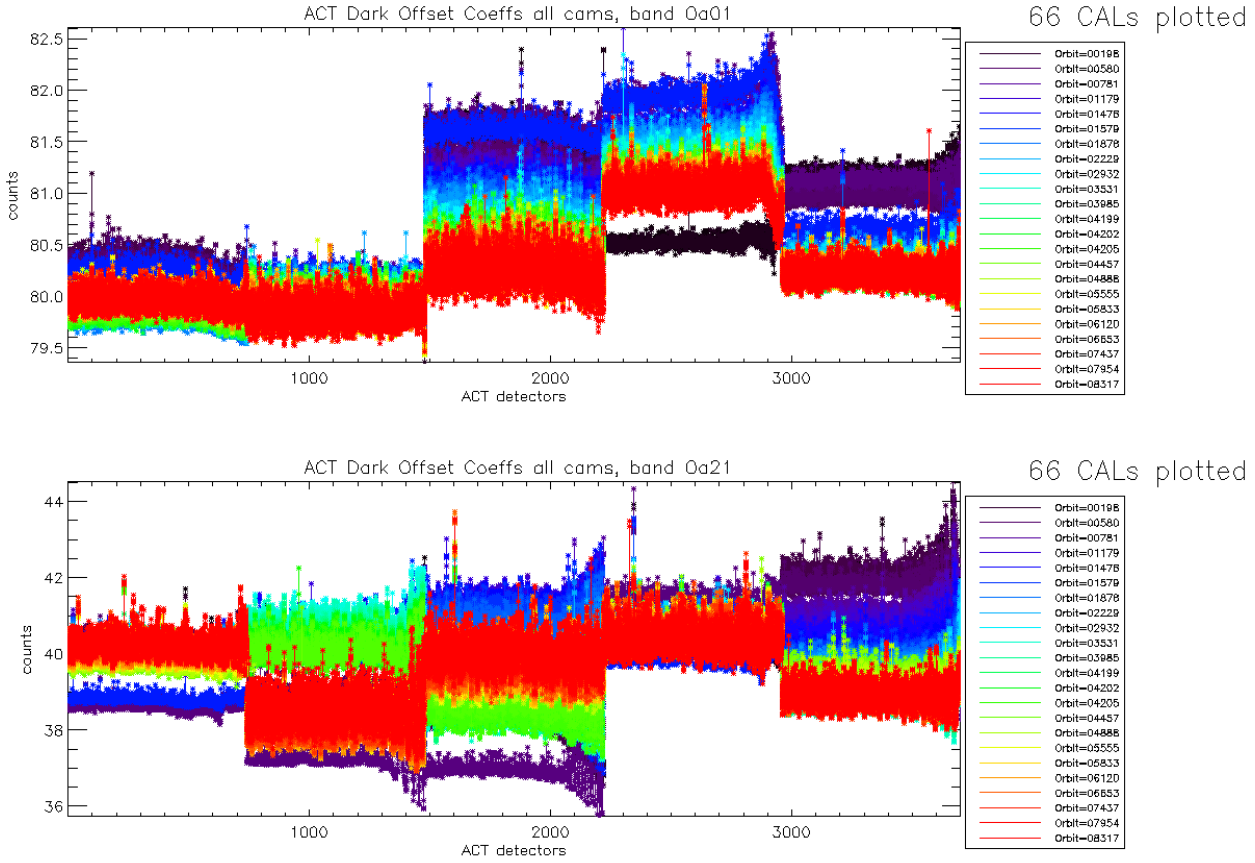

Figure 6: Dark Offset for band Oa1 (top) and Oa21 (bottom), all radiometric calibrations so far except the first one (orbit 183) for which the instrument was not thermally stable yet.

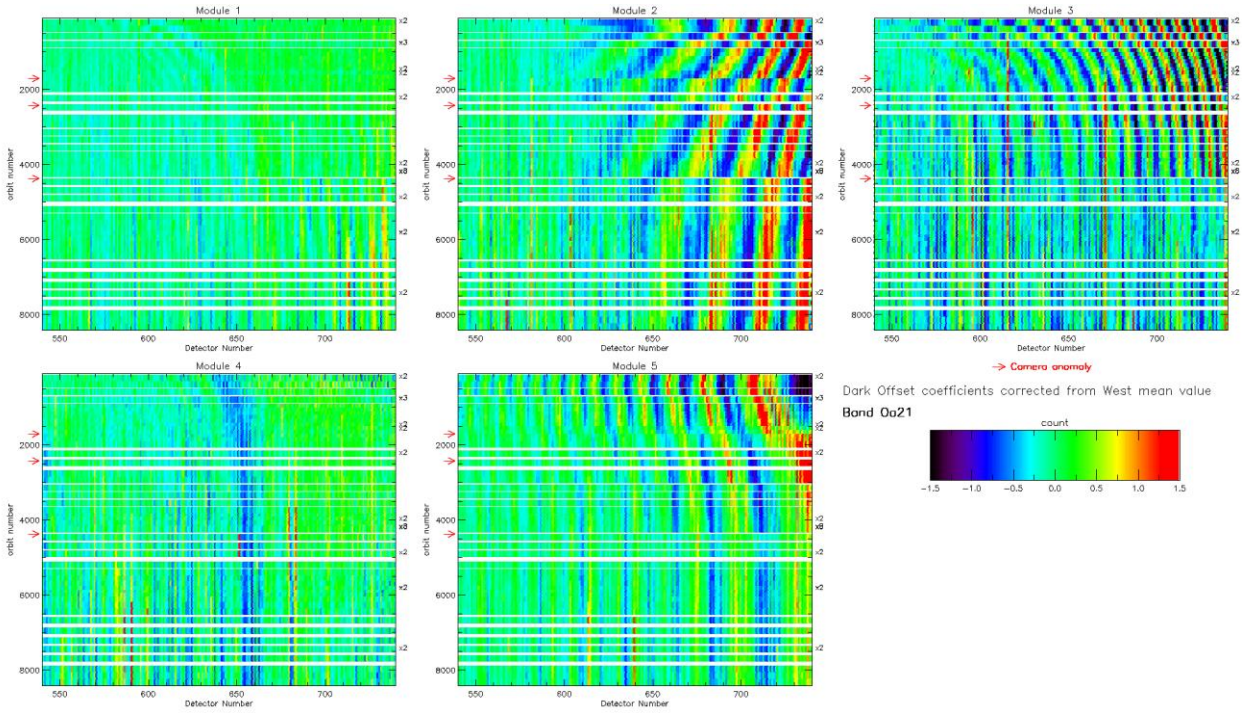

Figure 7: map of periodic noise for the 5 cameras, for band Oa21. X-axis is detector number (East part, from 540 to 740, where the periodic noise occurs), Y-axis is the orbit number. The counts have been corrected from the west detectors mean value (not affected by periodic noise) in order to remove mean level gaps and consequently to have a better visualisation of the long term evolution of the periodic noise structure. Periodic noise amplitude is high in camera 2, 3 and 4. It is lower in camera 4 and small in camera 1.

Looking at Figure 6 shows no significant evolution of this parameter during the current cycle. Figure 7 shows that since the last sudden PN change (phase and amplitude) caused by the camera-2 anomaly at orbit 4364 (18 December 2016), PN is nearly stabilized again. (See in particular cameras 3 & 5). However we can notice a small drift which is still present in camera 2.

Dark Currents

Dark Currents are not affected by the global offset of the Dark Offsets, thanks to the clamping to the average blind pixels value. However, the oscillations of Periodic Noise remain visible. There is no significant evolution of this parameter during the current cycle.

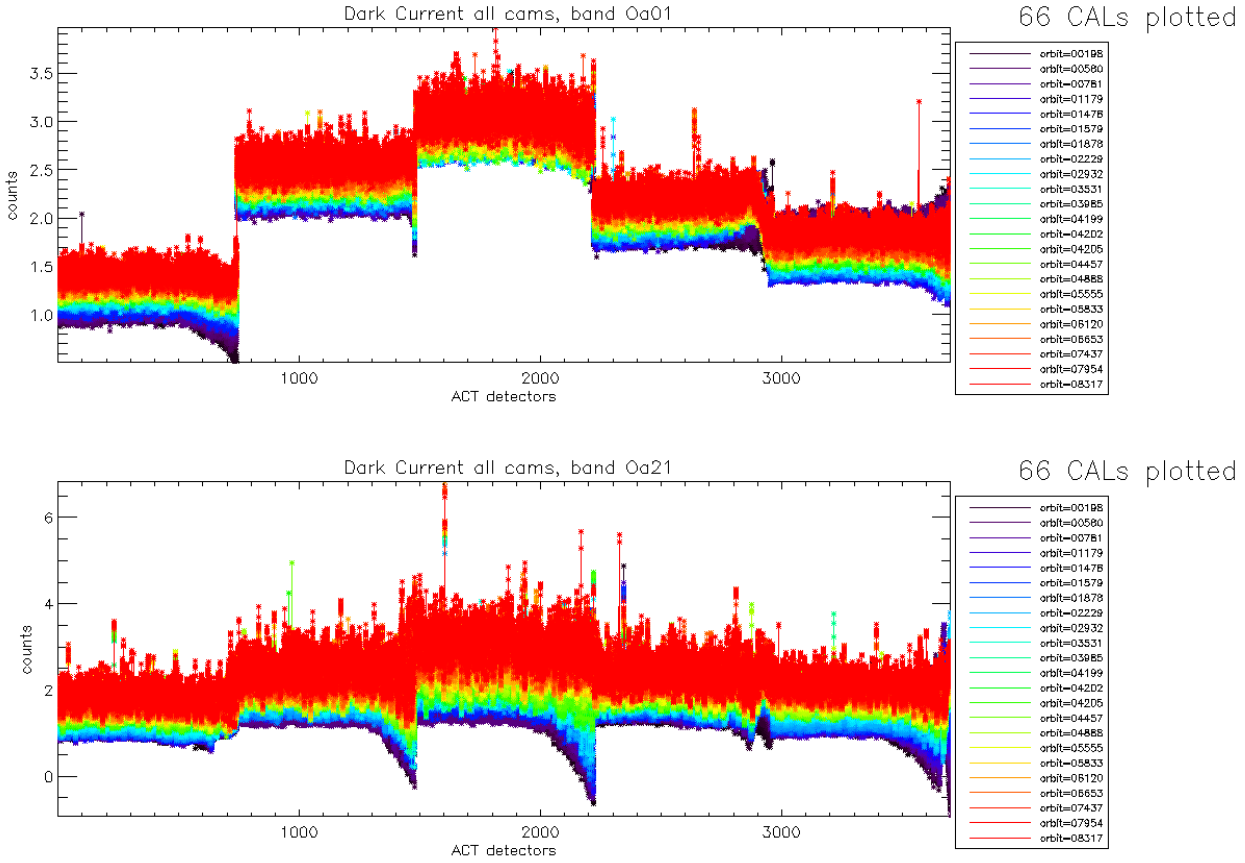

Figure 8: Dark Current for band Oa1 (top) and Oa21 (bottom), all radiometric calibrations so far except the first one (orbit 183) for which the instrument was not thermally stable yet.

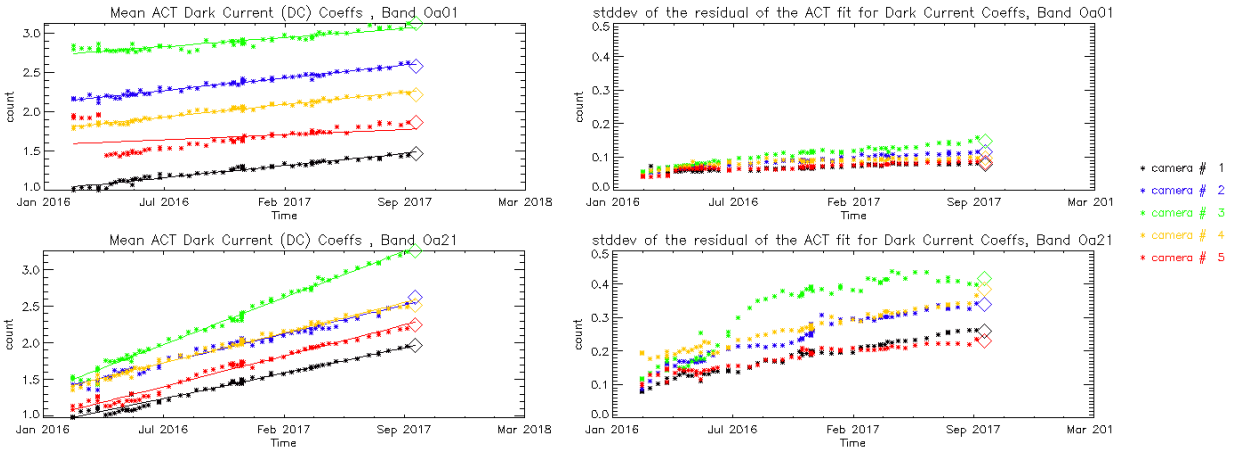

Figure 9: left column: ACT mean on 400 first detectors of Dark Current coefficients for spectral band Oa01 (top) and Oa21 (bottom). Right column: same as left column but for Standard deviation instead of mean. We see an increase of the DC level as a function of time especially for band Oa21. A possible explanation could be the increase of the number of hot pixels which is more important in Oa21 because this band is made of more CCD lines than band Oa01 and thus receives more cosmic rays impacts. It is known that cosmic rays degrade the structure of the CCD, generating more and more hot pixels at long term scales.

1.2.2 Instrument response and degradation modelling [OLCI-L1B-CV-250]

1.2.2.1 Instrument response monitoring

Figure 10 below shows the gain coefficients of every pixel for two OLCI channels, Oa1 (400 nm) and Oa21 (1020 nm), highlighting the significant evolution of the instrument response since early mission.

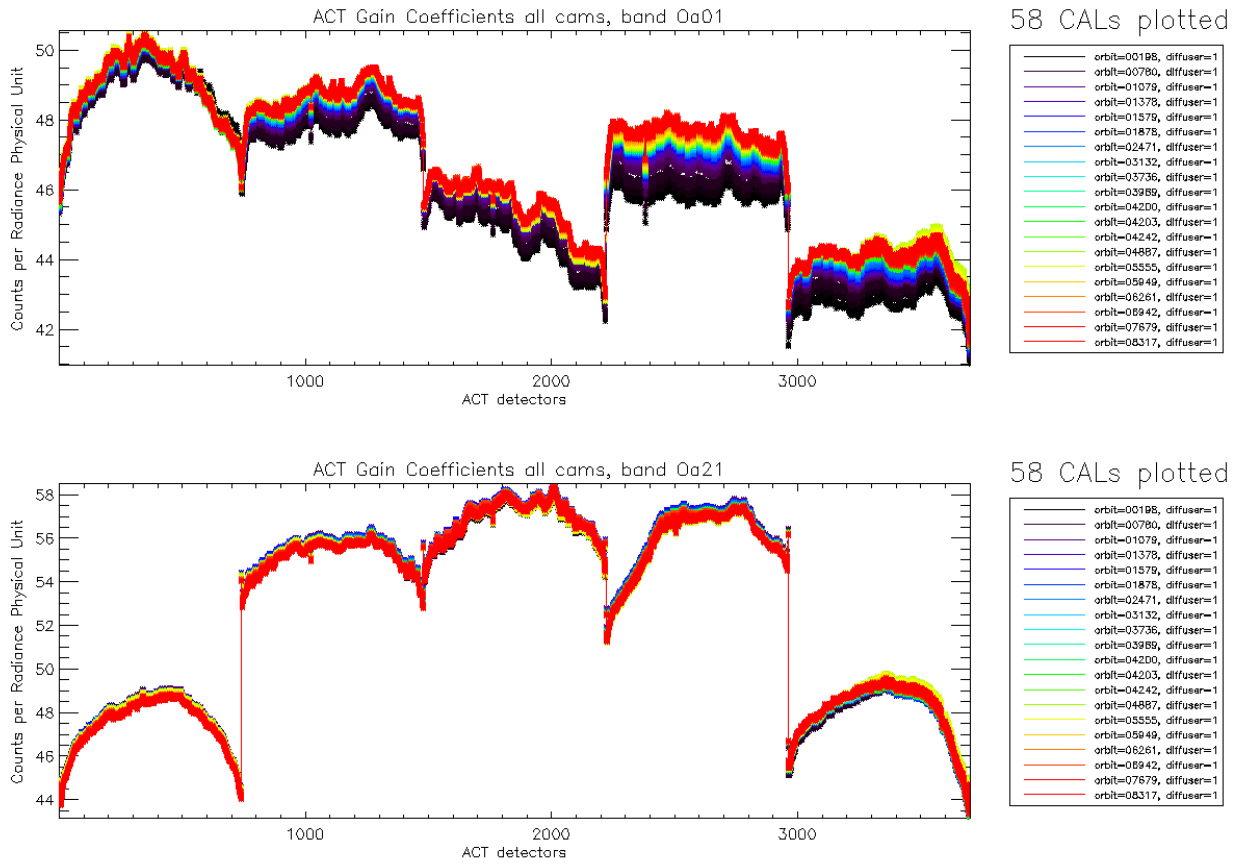

Figure 10: Gain Coefficients for band Oa1 (top) and Oa21 (bottom), all diffuser 1 radiometric calibrations so far except the first one (orbit 183) for which the instrument was not thermally stable yet.

The gains plotted in Figure 10, however are derived using the ground BRDF model – as the only one available in the operational processing software so far – which is known to suffer from illumination geometry dependent residual errors (see previous Cyclic Reports for more details). Consequently they are post-processed to replace the ground BRDF model by the in-flight version, based on Yaw Manoeuvres data, prior to determine the radiometric evolution.

Figure 11 displays a summary of the time evolution derived from post-processed gains: the cross-track average of the BRDF corrected gains is plotted as a function of time, for each module, relative to a given reference calibration (the 12/12/2016). It shows that, if a significant evolution occurred during the early mission, the trends tend to stabilize, with the exception of band 1 of camera 4.

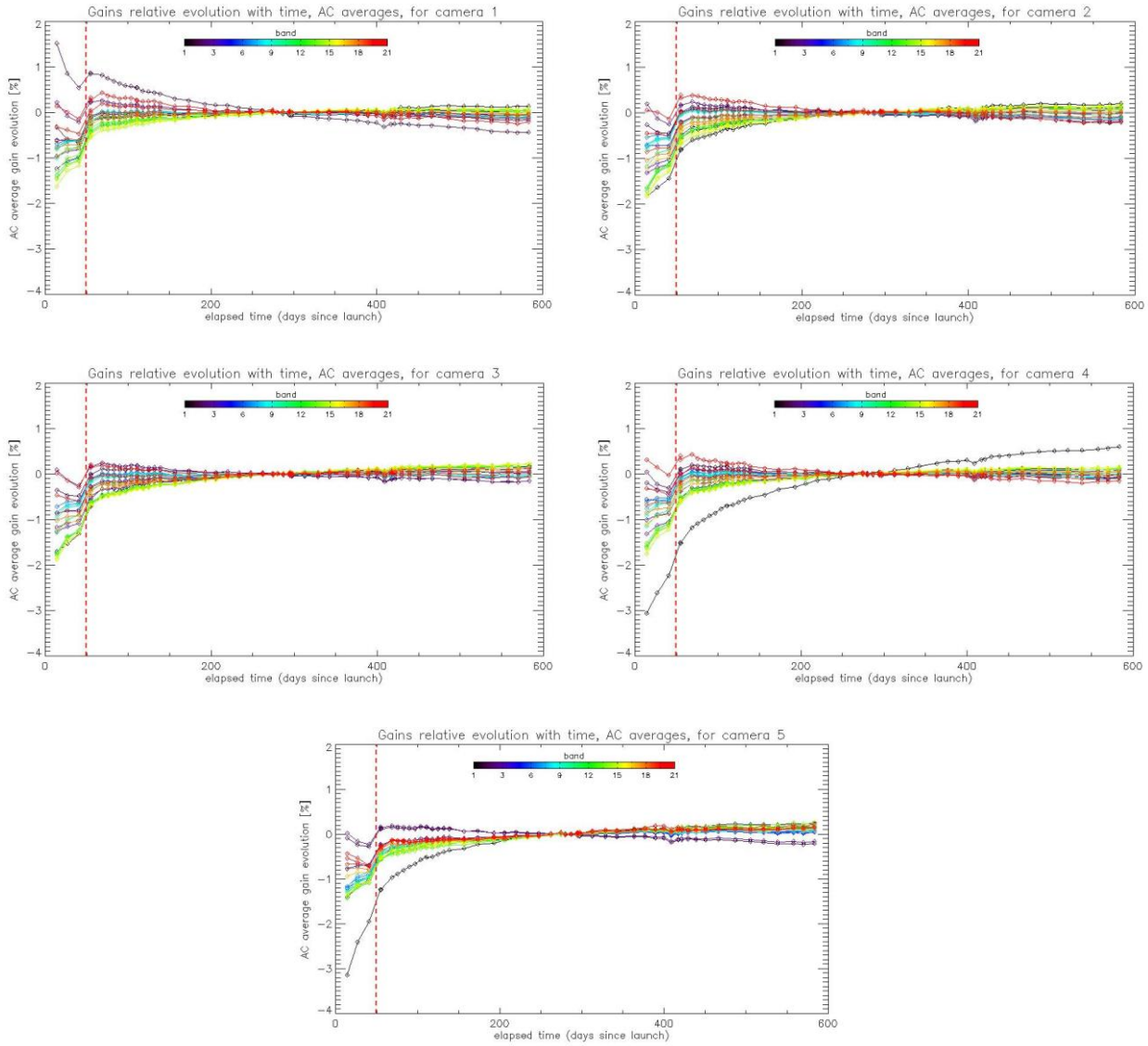

Figure 11: camera averaged gain relative evolution with respect to "best geometry" calibration (22/11), as a function of elapsed time since launch; one curve for each band (see colour code on plots), one plot for each module. The star tracker anomaly fix (6/04/16) is represented by a vertical red dashed line.

The behaviour over the first two months of mission, really different and highlighted by Figure 11, is explained by the Star Tracker software anomaly during which the attitude information provided by the platform was corrupted, preventing to compute a correct illumination geometry, with a significant impact on the gain computation.

1.2.2.2 Instrument evolution modelling

Thanks to the work done on the Yaw Manoeuvers Calibration acquisitions (see section 1.2.5) an upgraded diffuser BRDF model has been derived, allowing to get rid of the operational model dependency with Sun azimuth discussed above. This in turn allowed building a global gain database corrected for BRDF error residuals. This database (from 26/04/2016 to 12/03/2017) was used as the

basis for the derivation of a long-term radiometric drift model. Limitations of the available dataset at that time did not allow including a correction of diffuser ageing and have shown some limitations of the fitting method to correctly model the evolution for cameras/channels for which it is very small: in this case the signal to noise ratio (e. g. due to diffuser speckle) is not high enough and the fit parameters that provide the best match are not physical. As a consequence, it happens that, despite the model matches very well to the data, its use in extrapolation generates large drifts that are very unlikely to occur. A post-processing is thus necessary to identify and update those cases, and close monitoring is required to detect model drift from the actual data.

The validation dataset now includes 16 calibrations over 6.5 months for performance estimation, including the calibrations acquired during current cycle.

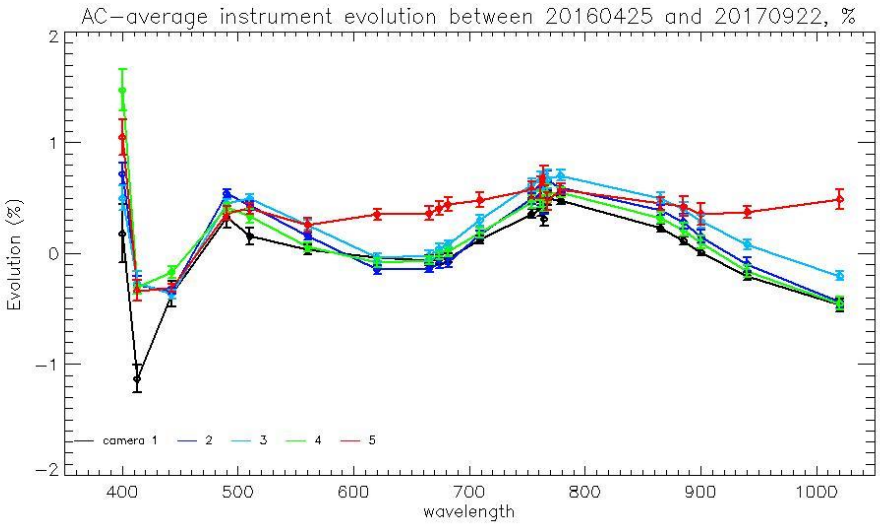

Figure 12: Camera-averaged instrument evolution since channel programming change (25/04/2016) and up to most recent calibration (22/09/2017) versus wavelength.

The model performance over the complete dataset (including the 16 calibrations in extrapolation over up to 6.5 months) remains better than 0.2% except at very specific cases: channel Oa1 of Camera 4 for recent calibrations, few isolated pixels in about half of the bands, and two specific features in camera 5 for channels Oa8 and Oa21 that cannot be fitted with a bounded exponential model. The overall performance at each orbit is shown on Figure 14 as the average and standard deviation of the model over data ratio as a function of wavelength, for each orbit in order to highlight a possible extrapolation issue. If the figure shows an outlying orbit, it must be stressed that it is NOT the most recent, excluding a systematic drift in extrapolation, as proved by Figure 15. Nevertheless, slow drift of the model with respect to data is observed, as shown on Figure 13, stressing the need for refreshing the model. This work has been completed during cycle 022, including correction of the ageing, and the resulting model is under validation for its use in both Operational Production and Global Reprocessing. A dedicated Verification Report will be issued in the coming days (S3MPC.ACR.VR.025). The new model is not discussed here as not yet in operation.

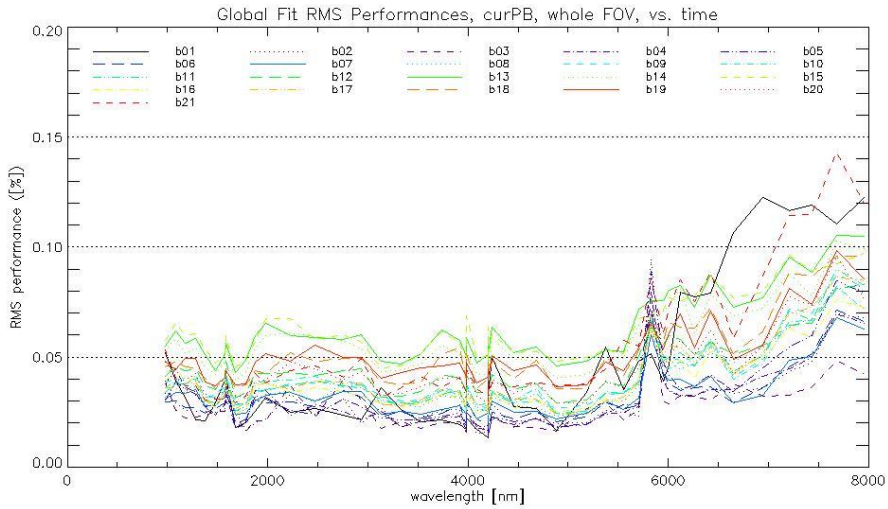

Figure 13: RMS performance of the Gain Model of current Processing Baseline as a function of orbit.

Finally, Figure 16 to Figure 18 show the detail of the model performance, with across-track plots of the model over data ratios at each orbit, one plot for each channel.

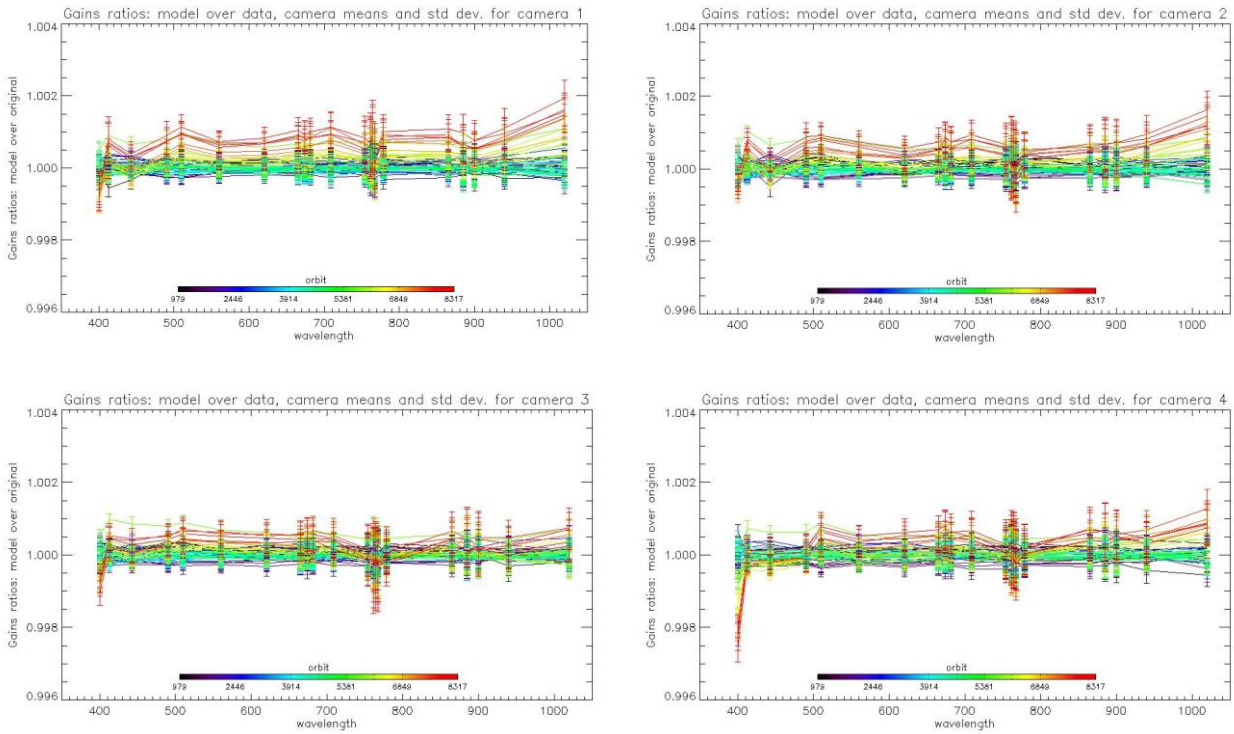

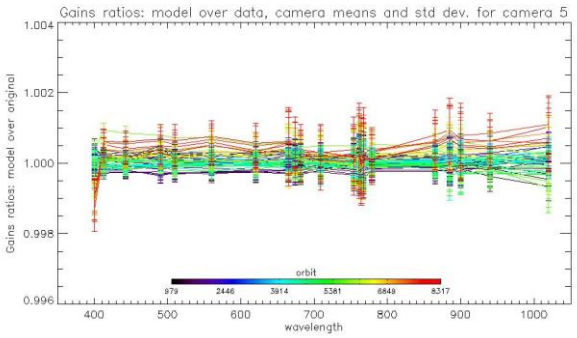

Figure 14: For the 5 cameras: Evolution model performance, as camera-average and standard deviation of ratio of Model over Data vs. wavelength, for each orbit of the test dataset, including 16 calibration in extrapolation, with a colour code for each calibration from blue (oldest) to red (most recent).

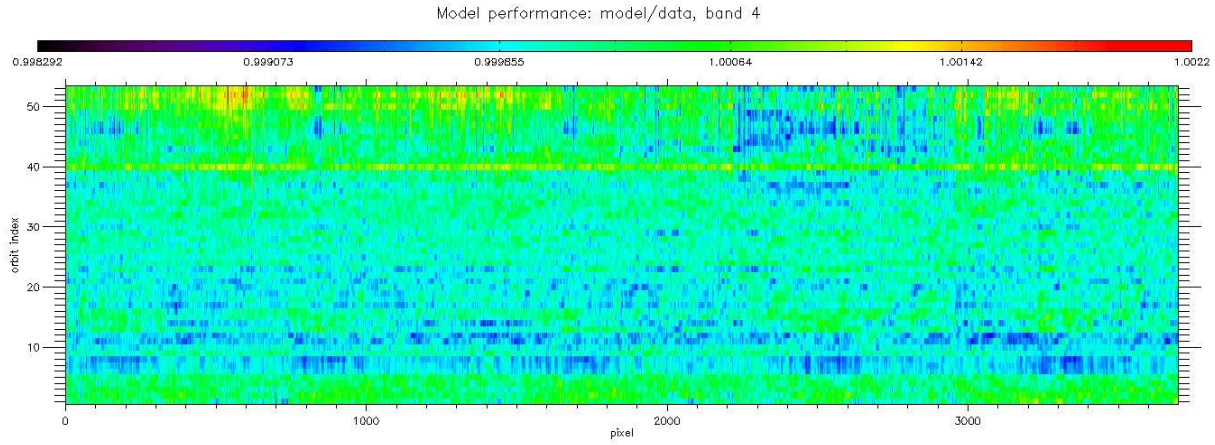

Figure 15: model performance: ratio of model over data for all pixels (x axis) of all orbits (y axis), for channel Oa4. The outlying orbit #40 is that of 31/03/2017.

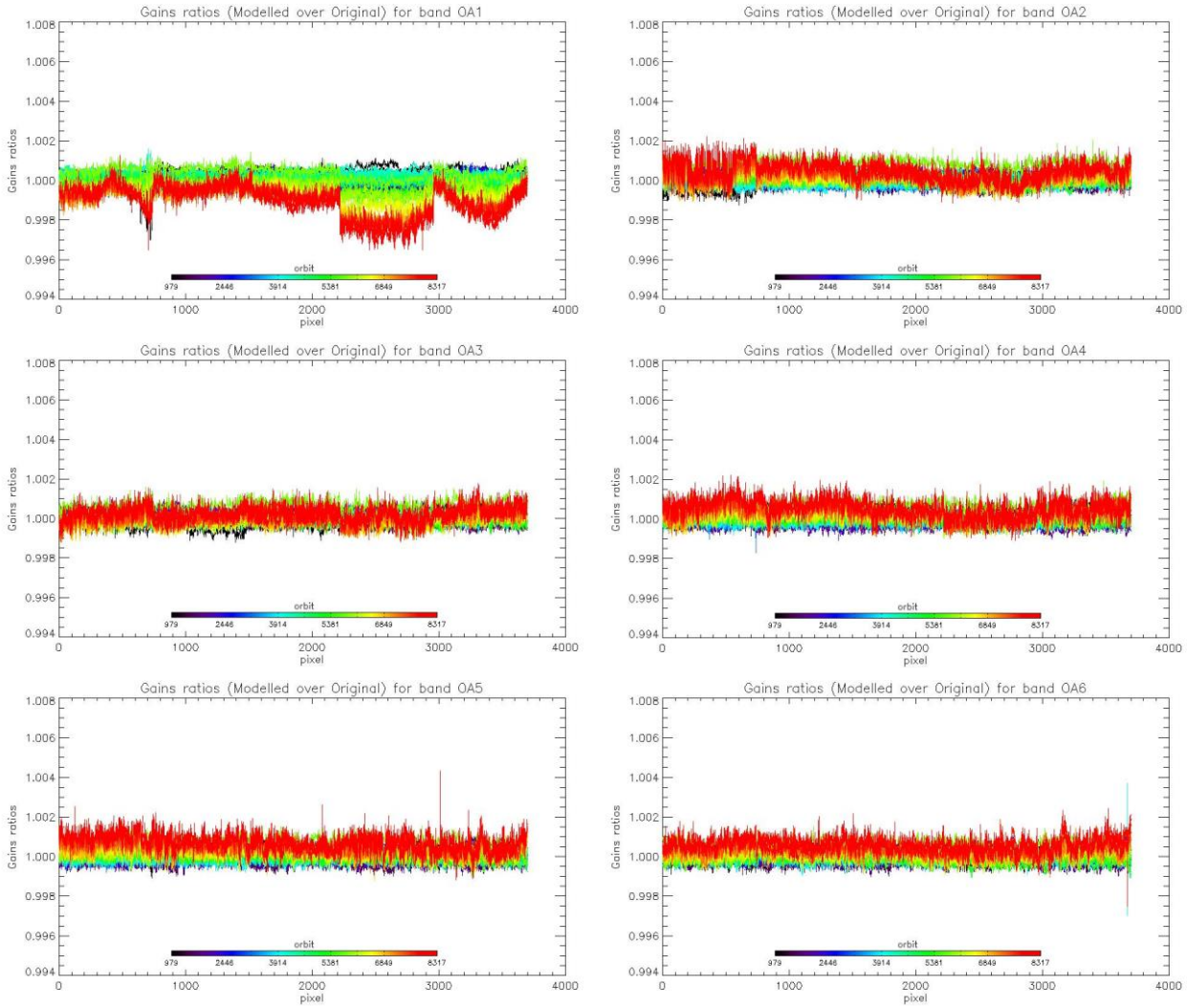

Figure 16: Evolution model performance, as ratio of Model over Data vs. pixels, all cameras side by side, over the whole current calibration dataset (since instrument programing update), including 16 calibration in extrapolation, channels Oa1 to Oa6.

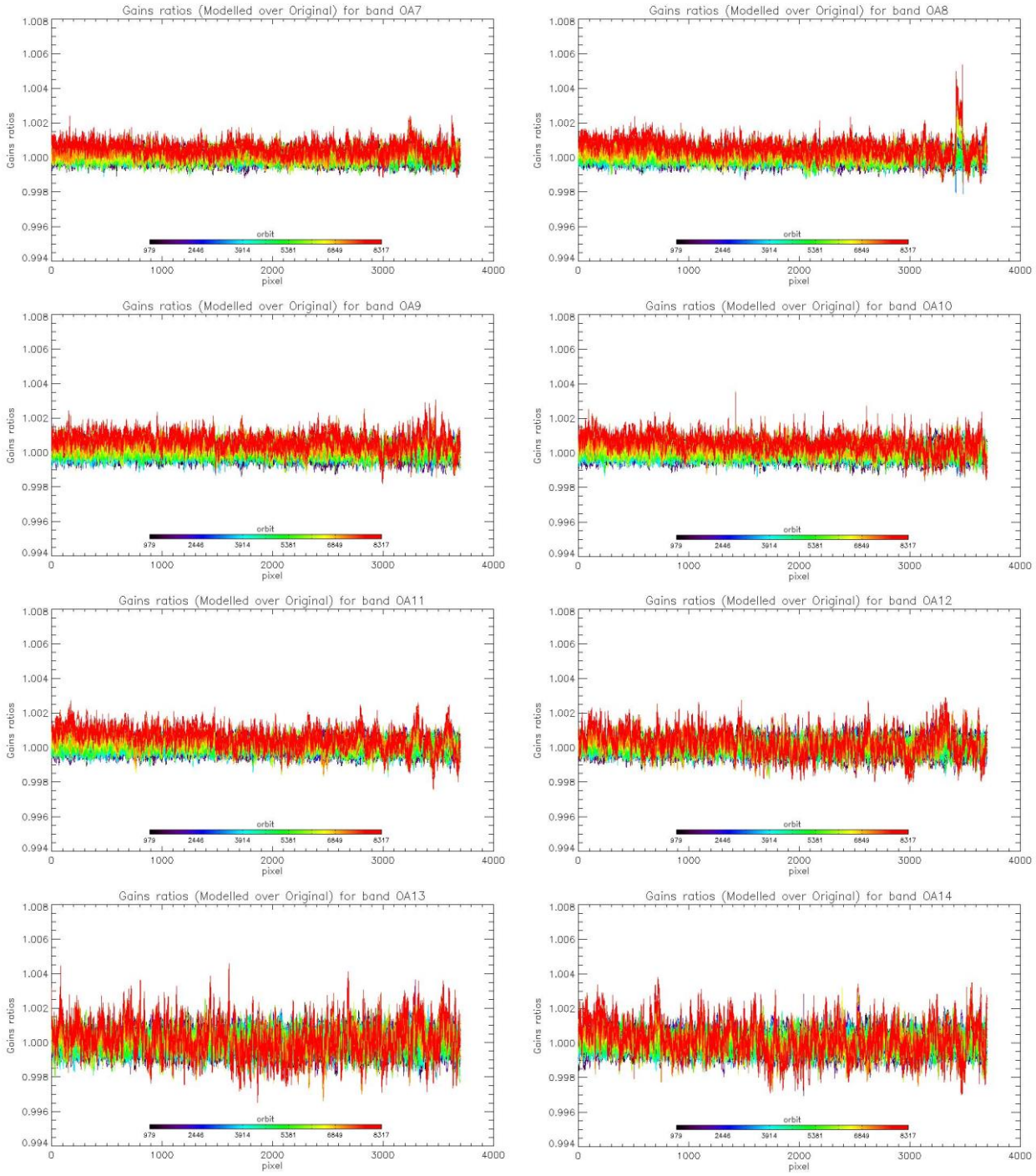

Figure 17: same as Figure 14 for channels Oa7 to Oa14.

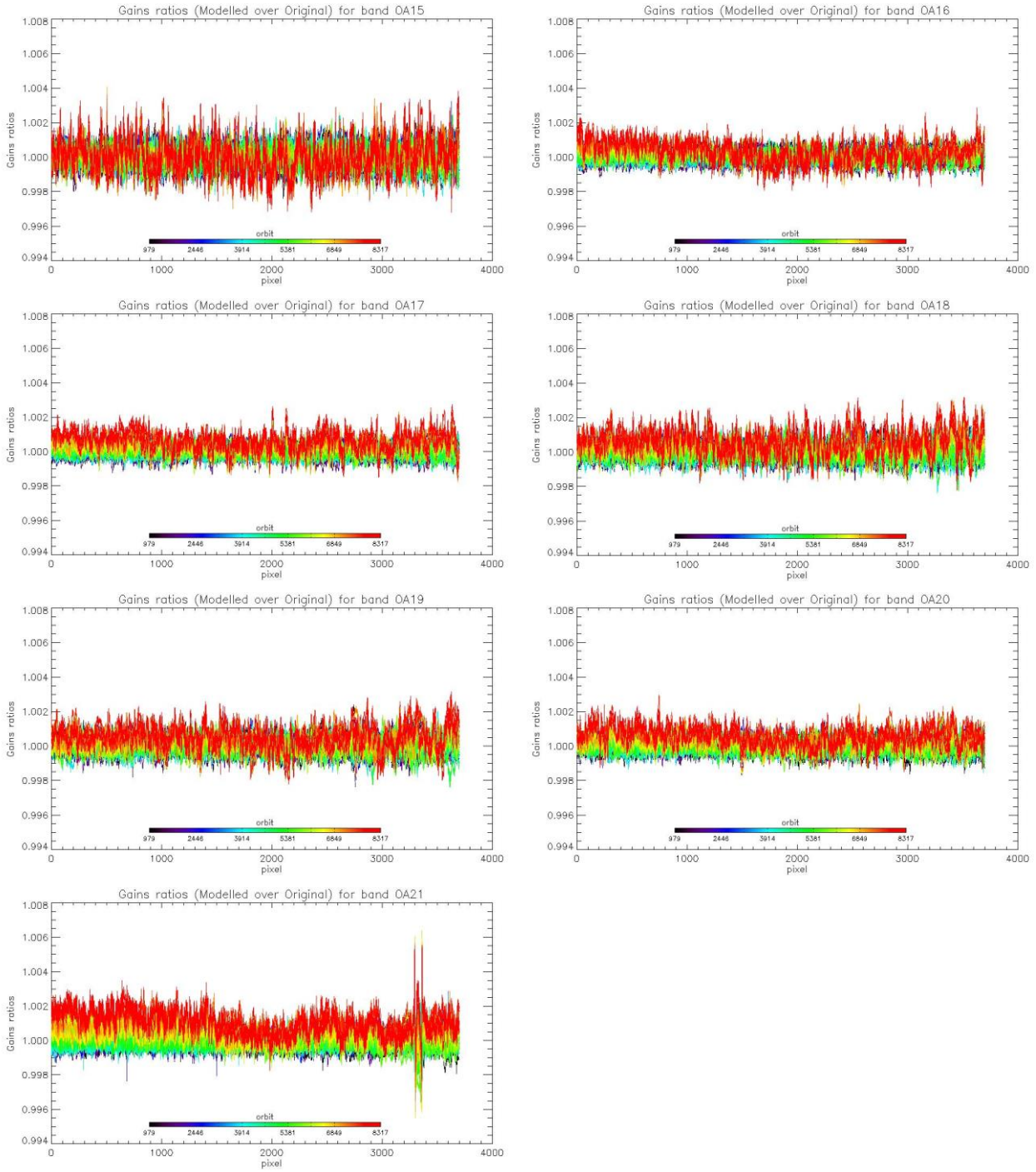

Figure 18: same as Figure 16 for channels Oa15 to Oa21.

1.2.3 Ageing of nominal diffuser [OLCI-L1B-CV-240]

There has been no calibration sequence S05 (reference diffuser) acquisition during cycle 022.

Consequently the last updated results (cycle 020) are still valid.

On the other hand, results of Cycle 020 have been used to derive a model of diffuser ageing as a function of cumulated exposure time (i.e. number of acquisition sequence on nominal diffuser, regardless of the band setting). This model has in turn been used to derive a new Gain Model, currently under validation. A dedicated Verification Report will be issued in the coming days (S3MPC.ACR.VR.025). The ageing model is not discussed here as not yet in operation.

1.2.4 Updating of calibration ADF [OLCI-L1B-CV-260]

A set of new calibration ADF has been generated, in view of the coming global reprocessing, to refresh the Dark Correction tables with HEP filtering (see above). These ADFs also include the updated Gain Model, accounting for all available RC up to cycle 21 and the ageing of the nominal diffuser. This model is not described in the present document that focuses on Operational Production but is the object of a dedicated report (S3MPC.ACR.VR.025).

S3A_OL_1_CAL_AX_20160425T103700_20160502T105515_20170914T101519_____MPC_O_AL_R03.SEN3
S3A_OL_1_CAL_AX_20160502T105515_20160509T111321_20170914T101519_____MPC_O_AL_R03.SEN3
S3A_OL_1_CAL_AX_20160509T111321_20160516T113134_20170914T101519_____MPC_O_AL_R03.SEN3
S3A_OL_1_CAL_AX_20160516T113134_20160523T100851_20170914T101519_____MPC_O_AL_R03.SEN3
S3A_OL_1_CAL_AX_20160523T100851_20160530T102711_20170914T101519_____MPC_O_AL_R03.SEN3
S3A_OL_1_CAL_AX_20160530T102711_20160606T104537_20170914T101519_____MPC_O_AL_R03.SEN3
S3A_OL_1_CAL_AX_20160606T104537_20160613T110409_20170914T101519_____MPC_O_AL_R03.SEN3
S3A_OL_1_CAL_AX_20160613T110409_20160620T112246_20170914T101519_____MPC_O_AL_R03.SEN3
S3A_OL_1_CAL_AX_20160620T112246_20160627T114128_20170914T101519_____MPC_O_AL_R03.SEN3
S3A_OL_1_CAL_AX_20160627T114128_20160704T101917_20170914T101519_____MPC_O_AL_R03.SEN3
S3A_OL_1_CAL_AX_20160704T101917_20160722T004742_20170914T101519_____MPC_O_AL_R03.SEN3
S3A_OL_1_CAL_AX_20160722T004742_20160808T014848_20170914T101519_____MPC_O_AL_R03.SEN3
S3A_OL_1_CAL_AX_20160808T014848_20160827T170709_20170914T101519_____MPC_O_AL_R03.SEN3
S3A_OL_1_CAL_AX_20160827T170709_20160909T094722_20170914T101519_____MPC_O_AL_R03.SEN3
S3A_OL_1_CAL_AX_20160909T094722_20160923T102636_20170914T101519_____MPC_O_AL_R03.SEN3
S3A_OL_1_CAL_AX_20160923T102636_20161007T092447_20170914T101519_____MPC_O_AL_R03.SEN3
S3A_OL_1_CAL_AX_20161007T092447_20161021T100350_20170914T101519_____MPC_O_AL_R03.SEN3
S3A_OL_1_CAL_AX_20161021T100350_20161104T190739_20170914T101519_____MPC_O_AL_R03.SEN3
S3A_OL_1_CAL_AX_20161104T190739_20161117T064426_20170914T101519_____MPC_O_AL_R03.SEN3
S3A_OL_1_CAL_AX_20161117T064426_20161122T061449_20170914T101519_____MPC_O_AL_R03.SEN3
S3A_OL_1_CAL_AX_20161122T061449_20161129T145852_20170914T101519_____MPC_O_AL_R03.SEN3
S3A_OL_1_CAL_AX_20161129T145852_20161207T062647_20170914T101519_____MPC_O_AL_R03.SEN3
S3A_OL_1_CAL_AX_20161207T062647_20161210T064921_20170914T101519_____MPC_O_AL_R03.SEN3
S3A_OL_1_CAL_AX_20161210T064921_20161225T084146_20170914T101519_____MPC_O_AL_R03.SEN3
S3A_OL_1_CAL_AX_20161225T084146_20170110T082623_20170914T101519_____MPC_O_AL_R03.SEN3
S3A_OL_1_CAL_AX_20170110T082623_20170124T122451_20170914T101519_____MPC_O_AL_R03.SEN3
S3A_OL_1_CAL_AX_20170124T122451_20170214T145948_20170914T101519_____MPC_O_AL_R03.SEN3
S3A_OL_1_CAL_AX_20170214T145948_20170227T123949_20170914T101519_____MPC_O_AL_R03.SEN3
S3A_OL_1_CAL_AX_20170227T123949_20170312T083848_20170914T101519_____MPC_O_AL_R03.SEN3
S3A_OL_1_CAL_AX_20170312T083848_20170322T142139_20170914T101519_____MPC_O_AL_R03.SEN3
S3A_OL_1_CAL_AX_20170322T142139_20170331T184952_20170914T101519_____MPC_O_AL_R03.SEN3

S3A_OL_1_CAL_AX_20170331T184952_20170408T234426_20170914T101519_____MPC_O_AL_R03.SEN3
S3A_OL_1_CAL_AX_20170408T234426_20170413T094608_20170914T101519_____MPC_O_AL_R03.SEN3
S3A_OL_1_CAL_AX_20170413T094608_20170420T233158_20170914T101519_____MPC_O_AL_R03.SEN3
S3A_OL_1_CAL_AX_20170420T233158_20170430T205014_20170914T101519_____MPC_O_AL_R03.SEN3
S3A_OL_1_CAL_AX_20170430T205014_20170512T135410_20170914T101519_____MPC_O_AL_R03.SEN3
S3A_OL_1_CAL_AX_20170512T135410_20170528T083518_20170914T101519_____MPC_O_AL_R03.SEN3
S3A_OL_1_CAL_AX_20170528T083518_20170617T145954_20170914T101519_____MPC_O_AL_R03.SEN3
S3A_OL_1_CAL_AX_20170617T145954_20170706T064231_20170914T101519_____MPC_O_AL_R03.SEN3
S3A_OL_1_CAL_AX_20170706T064231_20170722T080911_20170914T101519_____MPC_O_AL_R03.SEN3
S3A_OL_1_CAL_AX_20170722T080911_20170808T072916_20170914T101519_____MPC_O_AL_R03.SEN3
S3A_OL_1_CAL_AX_20170808T072916_20170827T142237_20170914T101519_____MPC_O_AL_R03.SEN3

1.2.5 Radiometric Calibrations for sun azimuth angle dependency and Yaw Manoeuvres for Solar Diffuser on-orbit re-characterization [OLCI-L1B-CV-270 and OLCI-L1B-CV-280]

This activity has not evolved during cycle 022 and results presented in previous report are still valid.

1.3 Spectral Calibration [OLCI-L1B-CV-400]

There has been no Spectral Calibration acquisitions sequence S02/S03 during cycle 022.

Consequently the last updated results (cycle 018) are still valid.

1.4 Signal to Noise assessment [OLCI-L1B-CV-620]

1.4.1 SNR from Radiometric calibration data.

SNR computed for all calibration data as a function of band number is presented in Figure 19.

SNR computed for all calibration data as a function of orbit number for band Oa01 (the less stable band) is presented in Figure 20.

There is no significant evolution of this parameter during the current cycle and the ESA requirement is fulfilled for all bands.

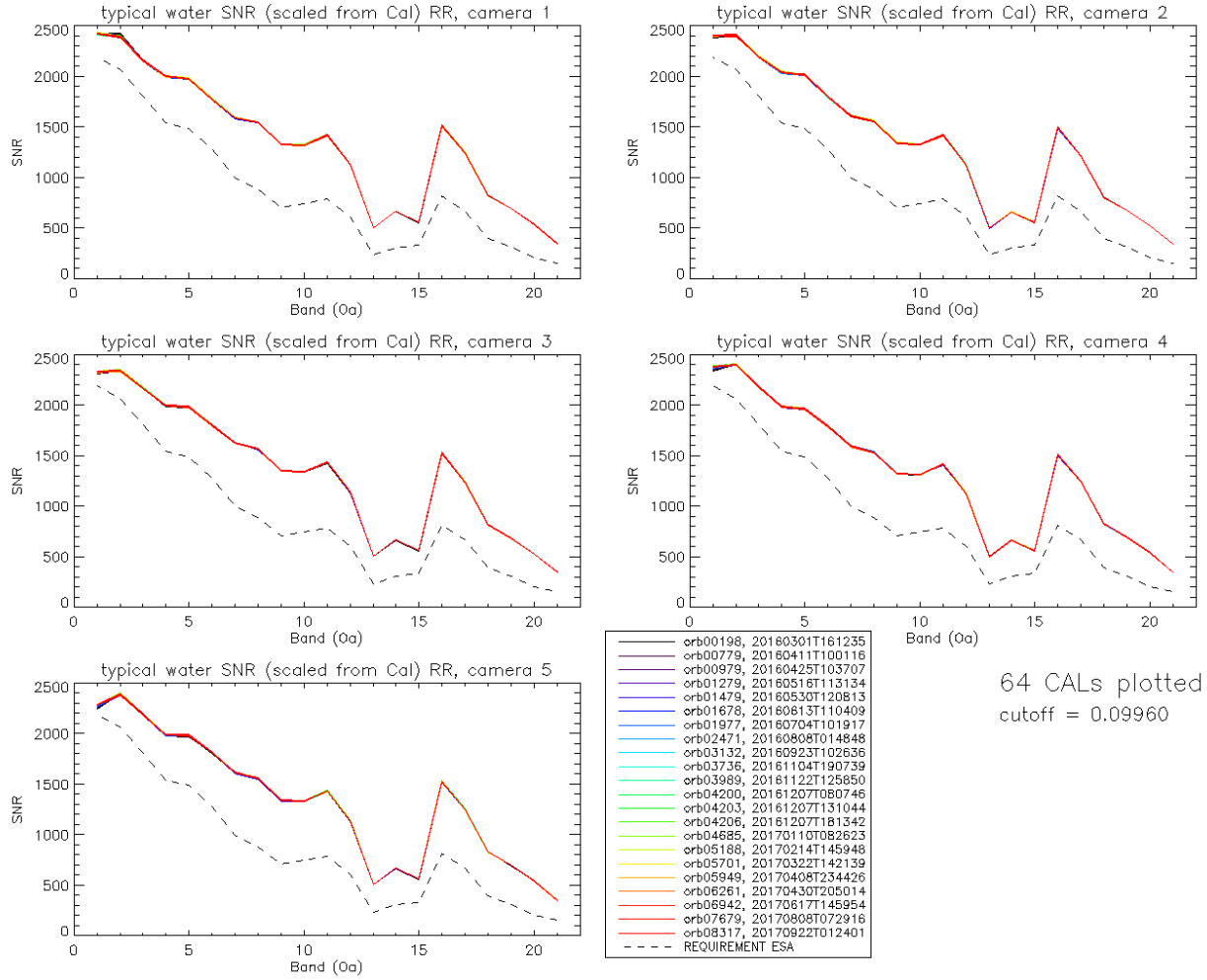

Figure 19: Signal to Noise ratio as a function of the spectral band for the 5 cameras. These results have been computed from radiometric calibration data. All calibrations except first one (orbit 183) are presents with the colours corresponding to the orbit number (see legend). The SNR is very stable with time: the curves for all orbits are almost superimposed. The dashed curve is the ESA requirement.

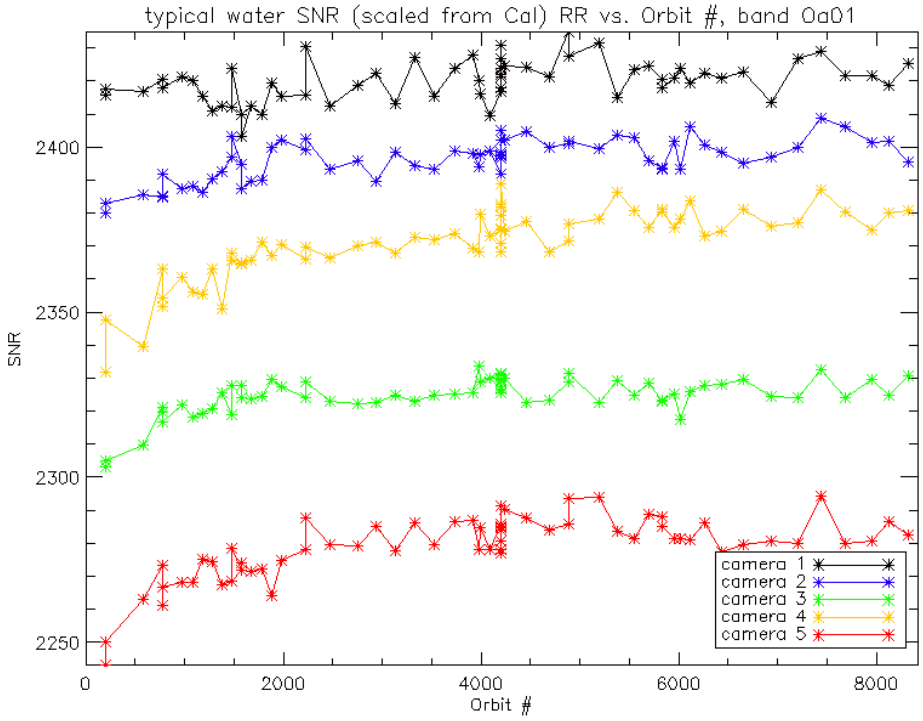

Figure 20: long-term stability of the SNR estimates from Calibration data, example of channel Oa1.

The mission averaged SNR figures are provided in Table 1 below, together with their radiance reference level. According to the OLCI SNR requirements, these figures are valid at these radiance levels and at Reduced Resolution (RR, 1.2 km). They can be scaled to other radiance levels assuming shot noise (CCD sensor noise) is the dominating term, i.e. radiometric noise can be considered Gaussian with its standard deviation varying as the square root of the signal; in other words: $SNR(L) = SNR(L_{ref}) \cdot \sqrt{\frac{L}{L_{ref}}}$. Following the same assumption, values at Full Resolution (300m) can be derived from RR ones as 4 times smaller.

Table 1: SNR figures as derived from Radiometric Calibration data. Figures are given for each camera (time average and standard deviation), and for the whole instrument. The requirement and its reference radiance level are recalled (in $mW.sr^{-1}.m^{-2}.nm^{-1}$).

λ	L_{ref}	SNR	C1		C2		C3		C4		C5		All	
nm	LU	RQT	avg	*std*	avg	*std*	avg	*std*	avg	*std*	avg	*std*	avg	*std*
400	*63*	*2188*	2420	*6.4*	2396	*6.1*	2324	*5.9*	2370	*10.9*	2278	*9.9*	2358	*6.4*
412.5	*74.1*	*2061*	2396	*8.4*	2409	*5.3*	2340	*4.8*	2402	*4.5*	2386	*7.3*	2386	*4.2*
442.5	*65.6*	*1811*	2161	*5.3*	2199	*5.8*	2167	*4.5*	2186	*4.4*	2197	*4.9*	2182	*3.4*
490	*51.2*	*1541*	1999	*5*	2035	*5.4*	1995	*3.6*	1981	*4*	1987	*5.1*	2000	*3.5*
510	*44.4*	*1488*	1979	*5.4*	2012	*4.9*	1982	*4.9*	1965	*4.5*	1984	*5*	1984	*3.9*
560	*31.5*	*1280*	1775	*4.4*	1801	*4.4*	1801	*4.9*	1793	*4*	1817	*3.8*	1798	*3.2*
620	*21.1*	*997*	1591	*4.2*	1609	*4.2*	1625	*3.3*	1593	*3.6*	1614	*3.7*	1606	*2.8*
665	*16.4*	*883*	1546	*4.6*	1558	*4.2*	1566	*3.8*	1532	*4.3*	1560	*3.9*	1552	*3.2*
673.75	*15.7*	*707*	1329	*3.4*	1338	*4*	1350	*2.9*	1323	*3*	1341	*4*	1336	*2.7*
681.25	*15.1*	*745*	1319	*3.7*	1326	*3.2*	1337	*3.1*	1314	*2.5*	1332	*3.9*	1326	*2.3*
708.75	*12.7*	*785*	1420	*4.6*	1420	*4.4*	1434	*3.8*	1413	*3.9*	1429	*3.1*	1423	*3.2*
753.75	*10.3*	*605*	1126	*3.5*	1119	*3.4*	1133	*3.9*	1123	*2.7*	1138	*3*	1128	*2.8*
761.25	*6.1*	*232*	501	*1.3*	498	*1.4*	504	*1.4*	500	*1.1*	507	*1.5*	502	*1.1*
764.375	*7.1*	*305*	662	*1.7*	657	*1.7*	667	*2.4*	660	*1.8*	669	*2.1*	663	*1.6*
767.5	*7.6*	*330*	558	*1.8*	554	*1.3*	561	*1.6*	556	*1.8*	563	*1.5*	558	*1.3*
778.75	*9.2*	*812*	1513	*5.4*	1496	*5.3*	1522	*5.5*	1509	*5.6*	1524	*5.2*	1513	*4.8*
865	*6.2*	*666*	1243	*3.8*	1212	*4.5*	1237	*4.4*	1245	*3.9*	1249	*2.9*	1237	*3.4*
885	*6*	*395*	823	*1.9*	801	*1.8*	813	*2.1*	824	*1.6*	830	*2*	818	*1.4*
900	*4.7*	*308*	691	*1.6*	673	*1.4*	683	*1.8*	692	*1.5*	697	*1.5*	687	*1.1*
940	*2.4*	*203*	534	*1*	522	*1.1*	525	*1*	539	*1.2*	542	*1.3*	532	*0.8*
1020	*3.9*	*152*	345	*0.8*	337	*0.7*	348	*0.7*	345	*0.8*	351	*0.7*	345	*0.5*

1.4.2 SNR from EO data.

There has been no update on SNR assessment from EO data during the cycle. Last figures (cycle 9) are considered valid.

1.5 Geometric Calibration/Validation

Regular monitoring using the GeoCal Tool implemented within the MPMF continues. Late August results confirm good performance. Monitoring of the geolocation performance by correlation with GCP imagettes using the GeoCal tool over the period confirms that OLCI is compliant with its requirement: the centroid of the geolocation error is around 0.2 to 0.3 pixel in both along-track and across-track directions (Figure 21 & Figure 22). The dispersion of the along-track errors in Figure 22 suggests

however that a per-camera analysis is required. Completion of the time series (started using the partial reprocessing dedicated to validation: 4 days every month between 26/04/16 and 12/03/2017) confirms the slow AL trend (Figure 23).

Performing additional geometric Calibration has to be done in a near future. This requires however using the GeoCal tool in Calibration mode, a mode that is not available in the GeoCal tool version implemented in the MPMF. Discussion has been started with ESTEC to see if their support can be envisaged.

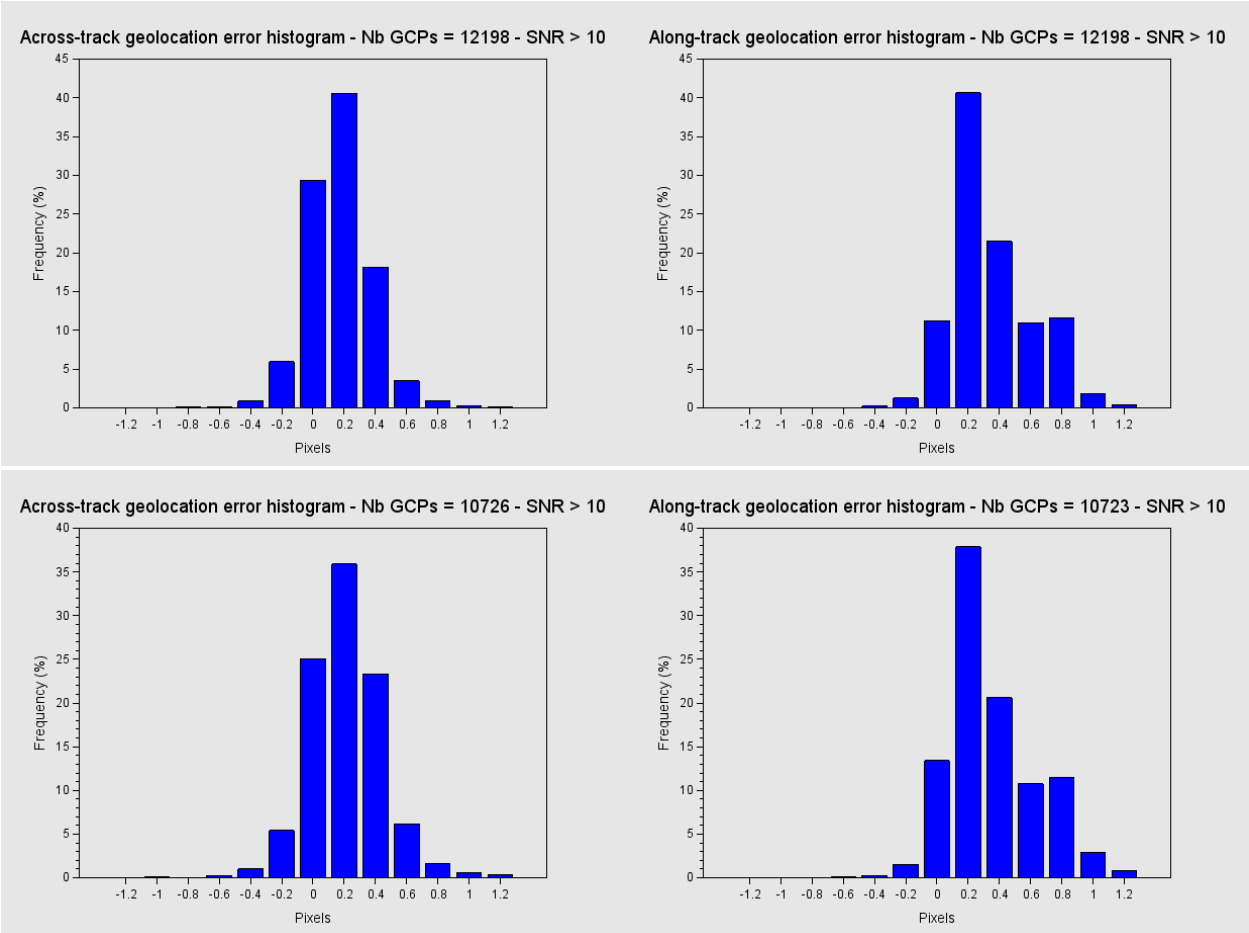

Figure 21: histograms of geolocation errors for the along-track (left) and across-track (right) directions, examples of 02/09/2017 (top) and 20/09/2017 (bottom).

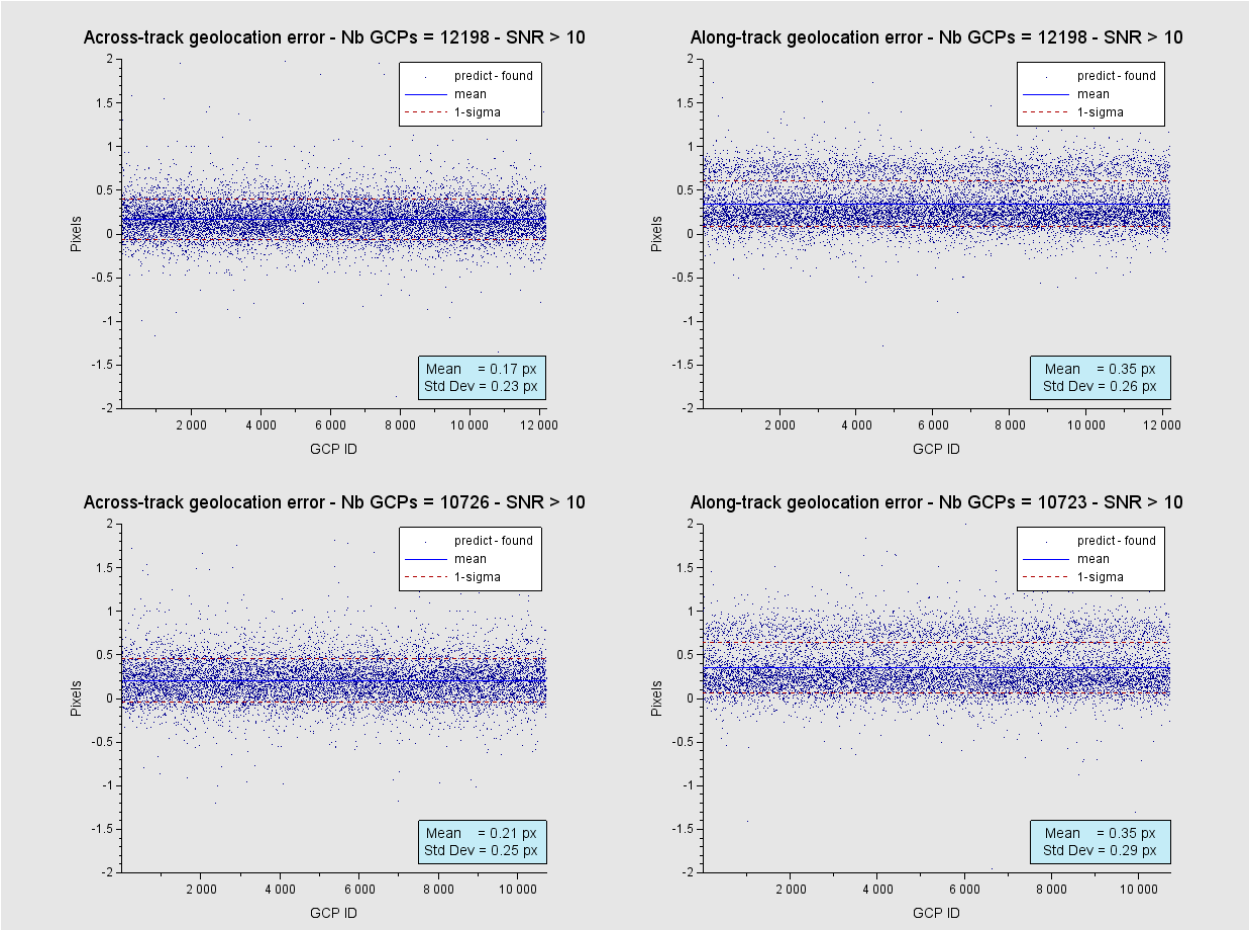

Figure 22: georeferencing error in along-track (left) and across-track (right) directions for all the GCPs, examples of 02/09/2017 (top) and 20/09/2017 (bottom).

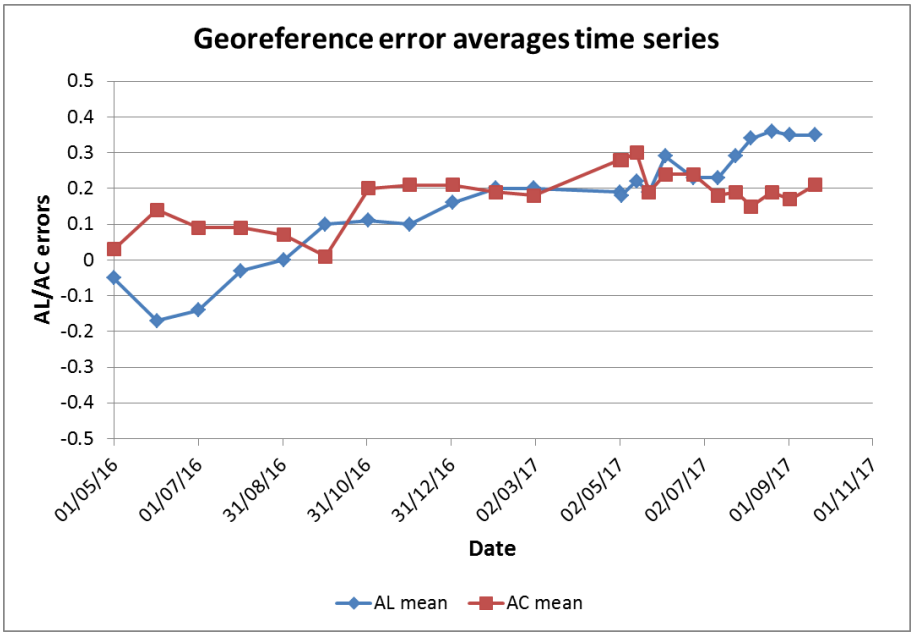

Figure 23: time series of geolocation errors for the along-track (blue) and across-track (red) directions over 15.6 months.

2 OLCI Level 1 Product validation

2.1 [OLCI-L1B-CV-300], [OLCI-L1B-CV-310] – Radiometric Validation

2.1.1 S3ETRAC Service

Activities done

The S3ETRAC service extracts OLCI L1 RR and SLSTR L1 RBT data and computes associated statistics over 49 sites corresponding to different surface types (desert, snow, ocean maximizing Rayleigh signal, ocean maximizing sunglint scattering and deep convective clouds). The S3ETRAC products are used for the assessment and monitoring of the L1 radiometry (optical channels) by the ESLs.

All details about the S3ETRAC/OLCI and S3ETRAC/SLSTR statistics are provided on the S3ETRAC website http://s3etrac.acri.fr/index.php?action=generalstatistics

- Number of OLCI products processed by the S3ETRAC service
- Statistics per type of target (DESERT, SNOW, RAYLEIGH, SUNGLINT and DCC)
- Statistics per sites
- Statistics on the number of records

For illustration, we provide below statistics on the number of S3ETRAC/OLCI records generated per type of targets (DESERT, SNOW, RAYLEIGH, SUNGLINT and DCC).

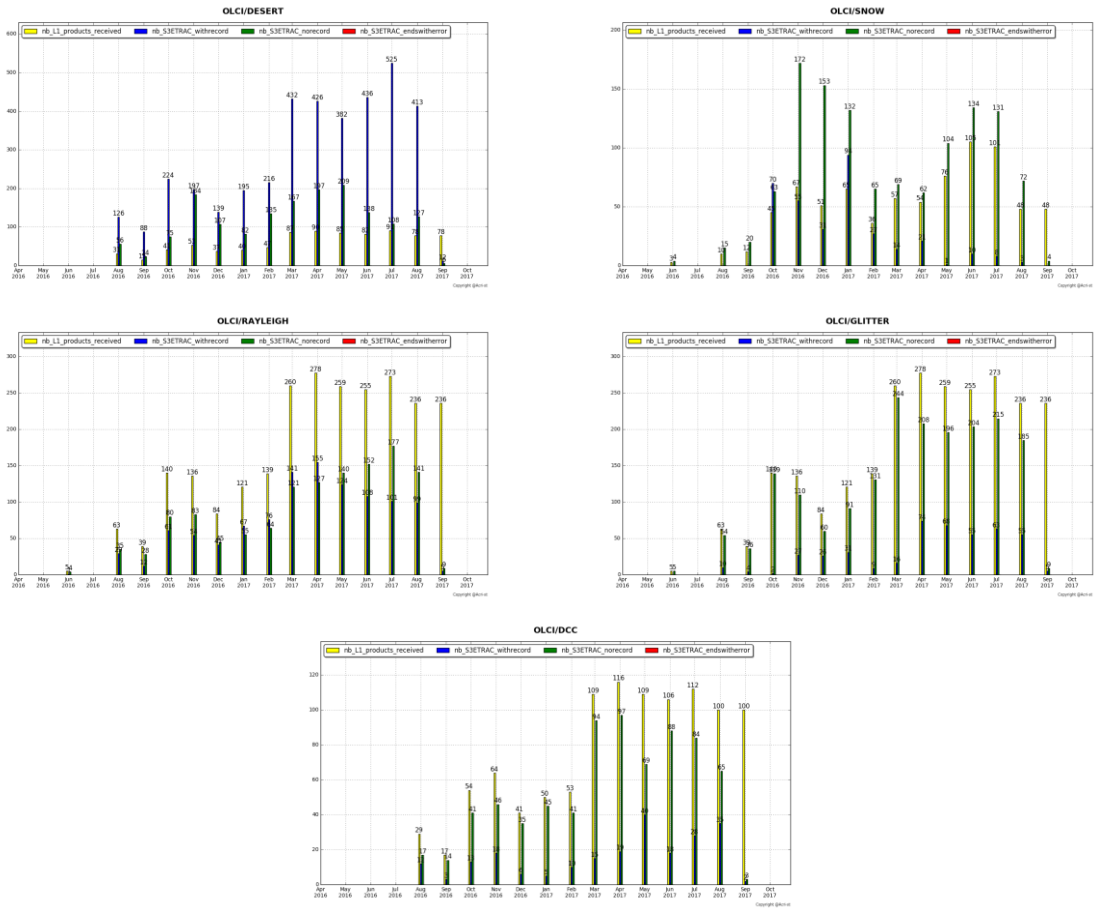

Figure 24: summary of S3ETRAC products generation for OLCI (number of OLCI L1 products Ingested, yellow – number of S3ETRAC extracted products generated, blue – number of S3ETRAC runs without generation of output product (data not meeting selection requirements), green – number of runs ending in error, red, one plot per site type).

2.1.2 Radiometric validation with DIMITRI

Highlights

- Run Rayleigh and Glint methods over the available products until 29th September.
- Run Desert method over the available products until 30th September 2017.
- About 40 new products from Cycle-22 were used in this analysis. The results are consistent with the previous cycle (Rayleigh, Glint and PICS).
- Good stability of the sensor could be observed, nevertheless, the time-series average shows higher reflectance over the VNIR spectral range with biases of 3%-5% except bands Oa06-Oa09
- Bands with high gaseous absorption are excluded.
- The results are consistent over the used CalVal sites

- The results need to be consolidated over ocean sites with more products from early mission period (before Dec 2016)..

I-Validation over PICS

1. Downloading and ingestion of all the available L1B-LN1-NT products in the S3A-Opt database over the 6 desert CalVal-sites (Algeria3 & 5, Libya 1 & 4 and Mauritania 1 & 2) has been performed until 30th September 2017.

2. The results are consistent overall the six used PICS sites (Figure 25). OLCI reflectance shows a good stability over the mission life-time.

3. The temporal average over the period **April 2016 – early October 2017** of the elementary ratios (observed reflectance to the simulated one) shows values higher than 2% (mission requirements) over all the VNIR bands (Figure 26). The spectral bands with significant absorption from water vapour and O_2 (Oa11, Oa13 and Oa14) show an outlier ratio.

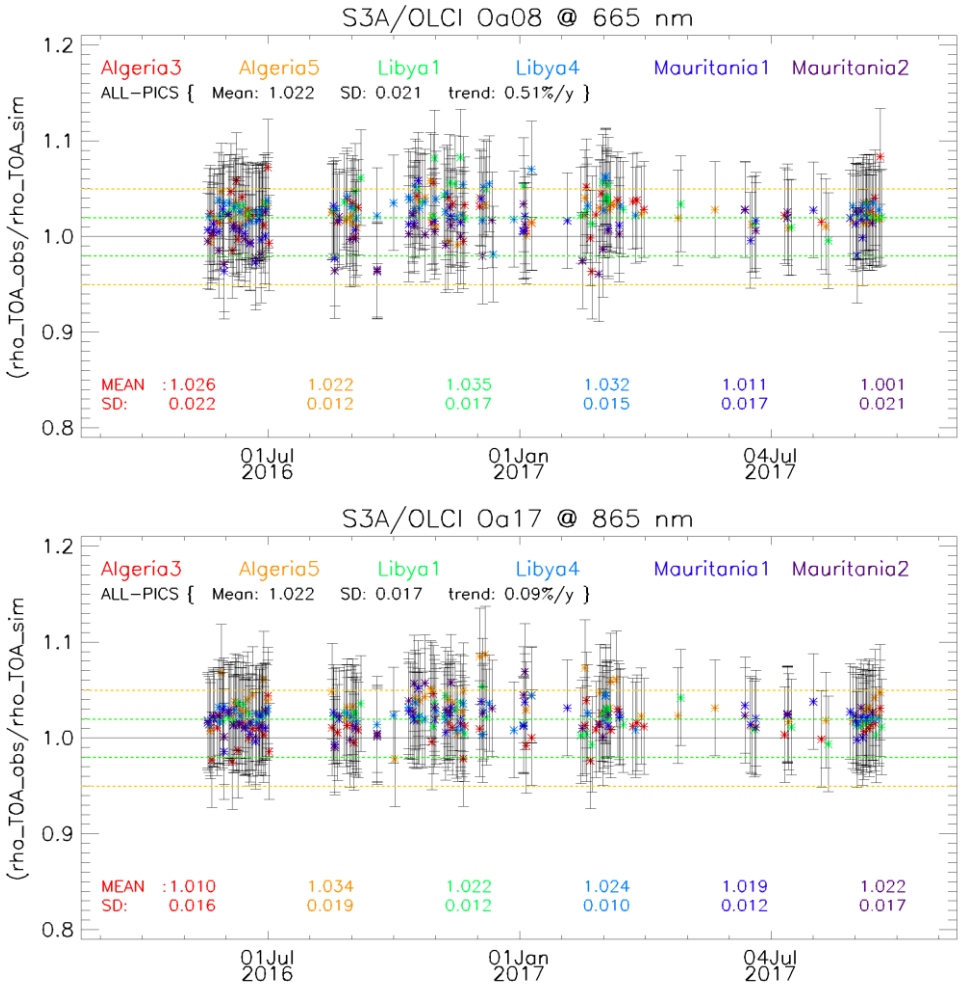

Figure 25: **Time-series of the elementary ratios (observed/simulated) signal from S3A/OLCI for (top to bottom) bands Oa03, Oa8 and Oa17 respectively over Six PICS Cal/Val sites. Dashed-green and orange lines indicate the 2% and 5% respectively. Error bars indicate the desert methodology uncertainty.**

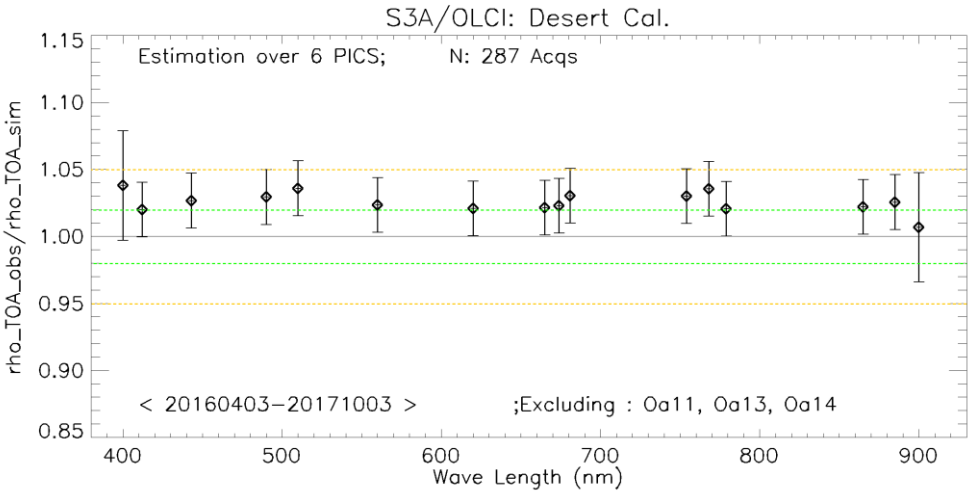

Figure 26: The estimated gain values for S3A/OLCI over the 6 PICS sites identified by CEOS over the period April 2016 – July 2017 as a function of wavelength. Dashed-green and orange lines indicate the 2% and 5% respectively. Error bars indicate the desert methodology uncertainty.

II-Intercomparison S3A/OLCI, S2A/MSI and LANDSAT/OLI over PICS

X-mission Intercomparison with MSI-A and MODIS-A is performed until September 2017. Figure 27 shows time-series of the elementary ratios from S2A/MSI and S3A/OLCI over LIBYA1 and LYBIA4 sites over the period April-2016 until September-2017.

We observe a clear stability over both sensors, associated with higher reflectance from OLCI wrt to MSI.

Figure 28 (not updated for Cycle-22) shows the estimated gain over the different time-series from different sensors (MODISA, MSIA, MSIB, OLCI and OLI) compared to the estimated gain over MERIS 3rd RP over PICS for the common bands between S2A/MSI, Aqua/MODIS and S3A/OLCI over ALGERIA5 and LIBYA1. Again Figure 27 confirms a systematic higher reflectance of OLCI wrt MSI and MODISA.

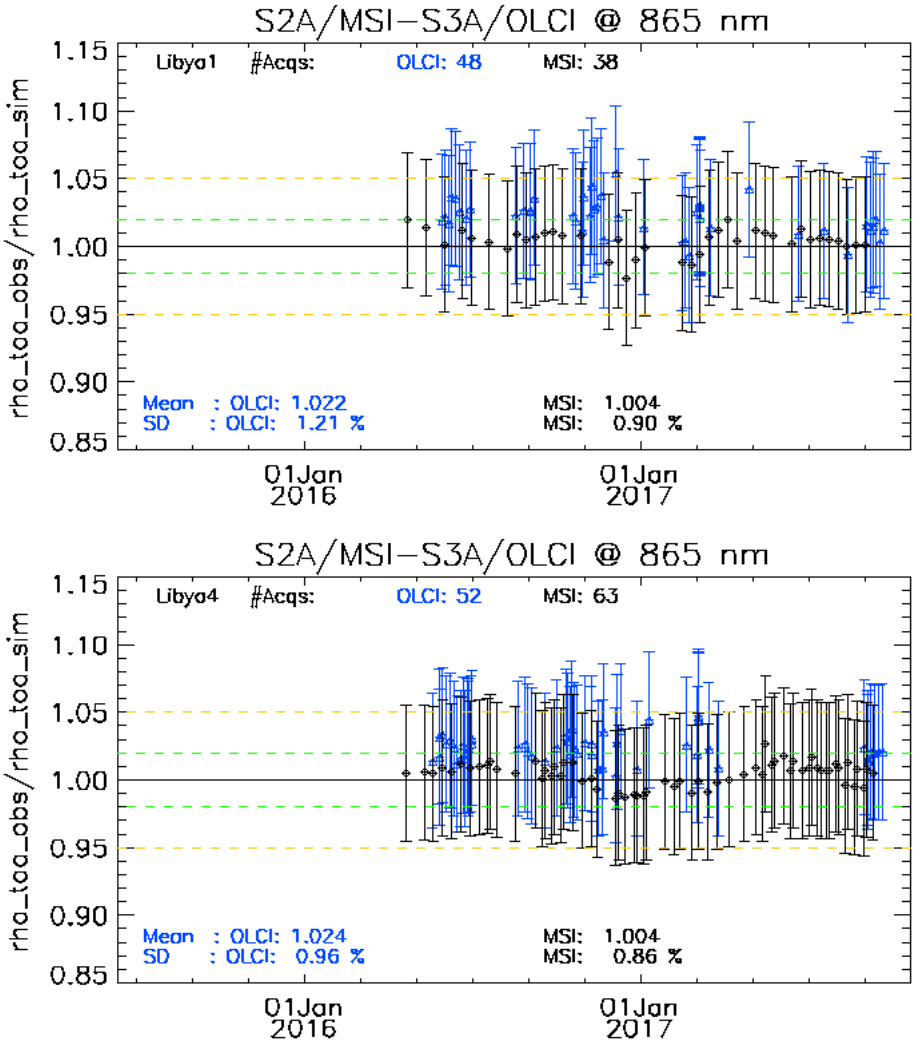

Figure 27: Time-series of the elementary ratios (observed/simulated) signal from (black) S2A/MSI, (blue) S3A/OLCI for band Oa17 (865nm) over LIBYA1 and LIBYA4 sites. Dashed-green and orange lines indicate the 2% and 5% respectively. Error bars indicate the desert methodology uncertainty.

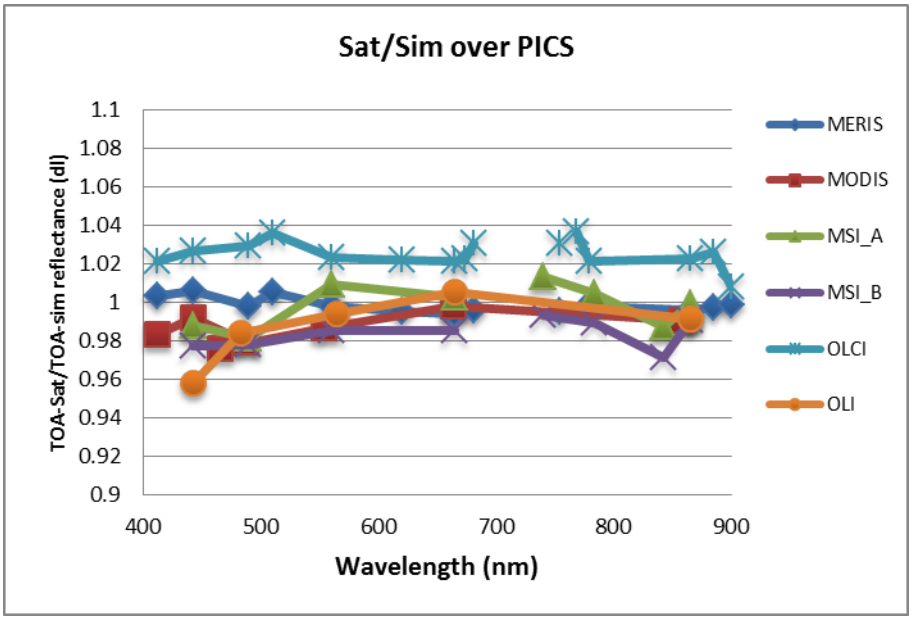

Figure 28: The estimated gain values (observed-signal /simulated-signal) averaged over different period from different sensors over PICS as function of wavelength.

III-Validation over Rayleigh

Rayleigh method has been performed over the available mini-files on the Opt-server until the cycle-22 period. The results produced with the configuration (ROI-AVERAGE) are consistent with the previous results of PICS method and from Cycles 20 & 21. While bands Oa01-Oa05 display a bias values between 2%-5%, bands Oa6-Oa9 exhibit biases within 2% (mission requirements) (Figure 29).

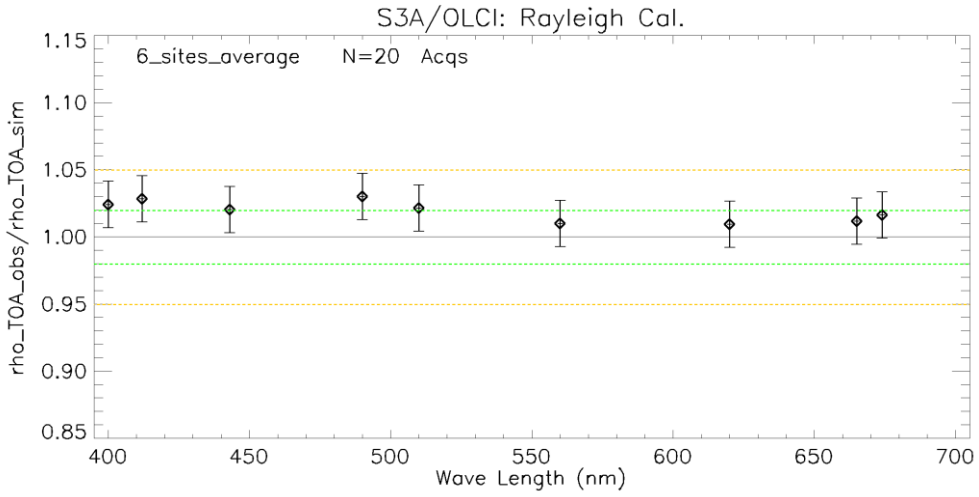

Figure 29: The estimated gain values for S3A/OLCI over the 6 Ocean CalVal sites (Atl-NW_Optimum, Atl-SW_Optimum, Pac-NE_Optimum, Pac-NW_Optimum, SPG_Optimum and SIO_Optimum) over the period December 2016 – September 2017 as a function of wavelength. Dashed-green, and orange lines indicate the 2%, 5% respectively. Error bars indicate the methodology uncertainty.

IV-Validation over Glint

Glint calibration method with the configuration (ROI-PIXEL) has been performed over the period December 2016 – end September 2017 from the available mini-files. The outcome of this analysis shows a good consistency with Rayleigh and the desert outputs over the NIR spectral range (see Figure 30).

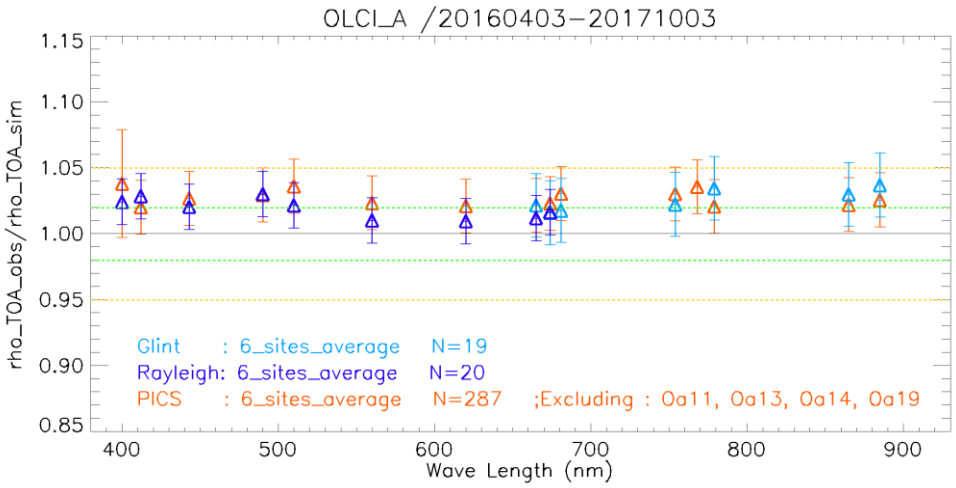

Figure 30: The estimated gain values for S3A/OLCI from Glint, Rayleigh and PICS over the period April 2016 – September 2017 for PICS and December 2016-September 2017 for Rayleigh and Glint methods as a function of wavelength. We use the gain value of Oa8 from PICS method as reference gain for Glint. Dashed-green and orange lines indicate the 2% and 5% respectively. Error bars indicate the methods uncertainties.

2.1.3 Radiometric validation with OSCAR

Preliminary (processing only partial finished) OSCAR Rayleigh results for July and August are given in Figure 31. The weighted average result over all Rayleigh sites is given for observations with an air mass factor larger than respectively 2 and 3. As can be seen in the figure the selection of valid pixels based on the air mass has an effect in the first 3 OLCI bands which illustrates the larger uncertainty of the Rayleigh results in these 3 bands.

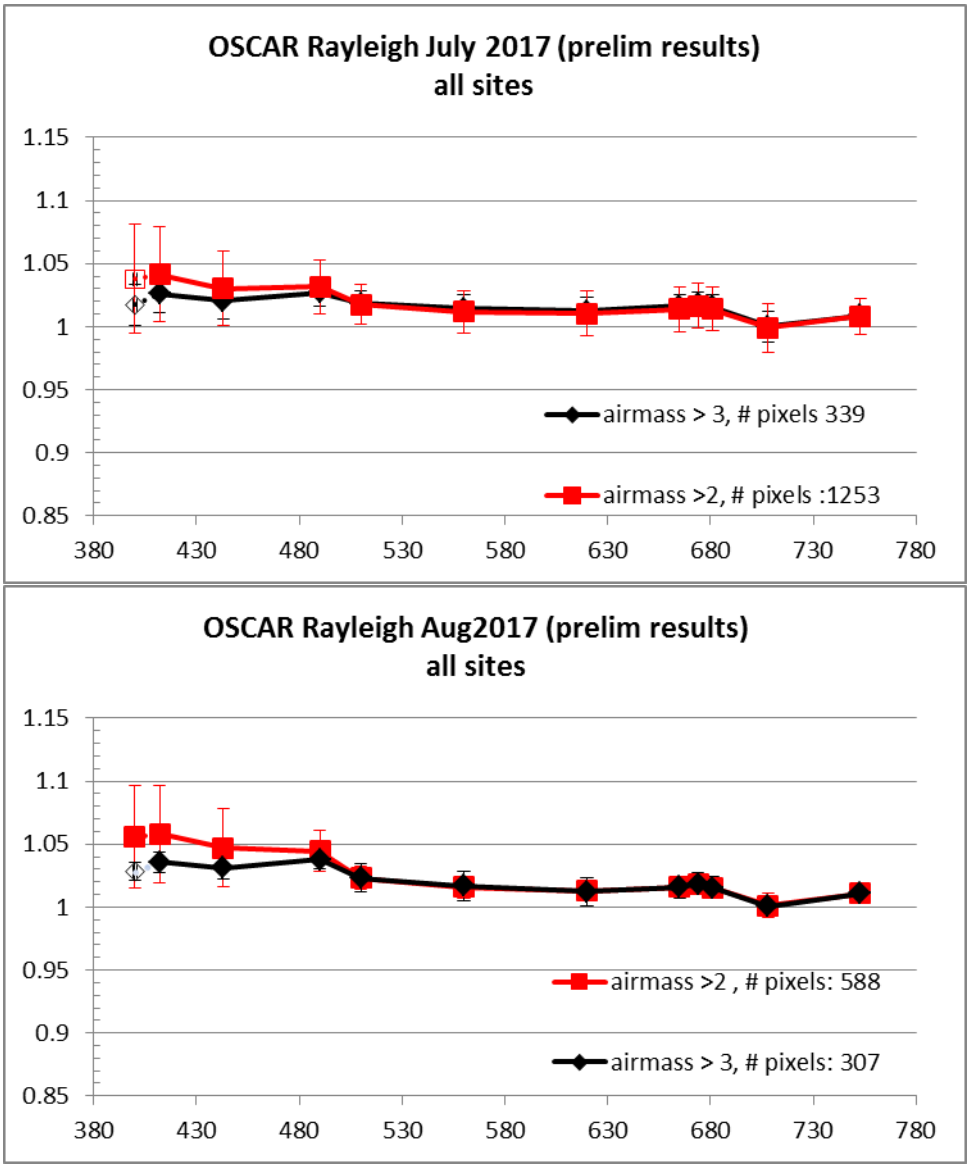

Figure 31: OSCAR Rayleigh results for July and Agust 2017.

2.2 [OLCI-L1B-CV-320] – Radiometric Validation with Level 3 products

There has been no new result during the cycle. Last figures (cycle 20) are considered valid

3 Level 2 Land products validation

3.1 [OLCI-L2LRF-CV-300]

There has been no new result during the cycle. Last figures (cycle 21) are considered valid

3.2 [OLCI-L2LRF-CV-410 & OLCI-L2LRF-CV-420] – Cloud Masking & Surface Classification for Land Products

There has been no update on Cloud Masking & Surface Classification for Land t during the cycle. Last figures (cycle 20) are considered valid.

3.3 Validation of Integrated Water Vapour over Land

There has been no update on Integrated Water Vapour over Land validation quantitative assessment during the cycle. Last figures (cycle 15) are considered valid.

Qualitative assessment by product inspection showed no detectable performance evolution.

4 Level 2 Water products validation

4.1 [OLCI-L2-CV-210, OLCI-L2-CV-220] – Vicarious calibration of the NIR and VIS bands

There has been no update on SVC (System Vicarious Calibration) during Cycle 022.

4.2 [OLCI-L2WLR-CV-300, OLCI-L2WLR-CV-310, OLCI-L2WLR-CV-32, OLCI-L2WLR-CV-330, OLCI-L2WLR-CV-340, OLCI-L2WLR-CV-350, OLCI-L2WLR-CV-360 and OLCI-L2WLR-CV-370] – Level 2 Water-leaving Reflectance product validation.

Activities done

- The focus for this time period has been on the Near Real Time data.
- All extractions and statistics have been regenerated for the last three months (July 1st 2017 onward; rolling archive limitation). The available matchups therefore cover the summer situation. Time range available for last processing period covered July 1st to September 29th
- An MPMF data provision failure has is not yet fully resolved. The amount of available data for routine validation is therefore very limited.
- Only a few matchups with AERONET-OC stations are available for this time period. These stations are located in optically complex waters (Baltic Sea, North Sea and gulf of California).

Overall Water-leaving Reflectance performance

Figure 32 and Figure 33 below presents the scatterplots with statistics of OLCI FR and RR versus in situ reflectance computed for the NRT dataset. The data considered correspond to the latest processing baseline ie including SVC. Owing to the on-going data provision issue, very few OLCI images and therefore matchups are available for this reporting period. No reliable interpretation can be derived from these statistics. Table 2 to Table 7 below summarises the statistics over the previous period. The statistics of the current NRT period are not presented in this report as considered not reliable.

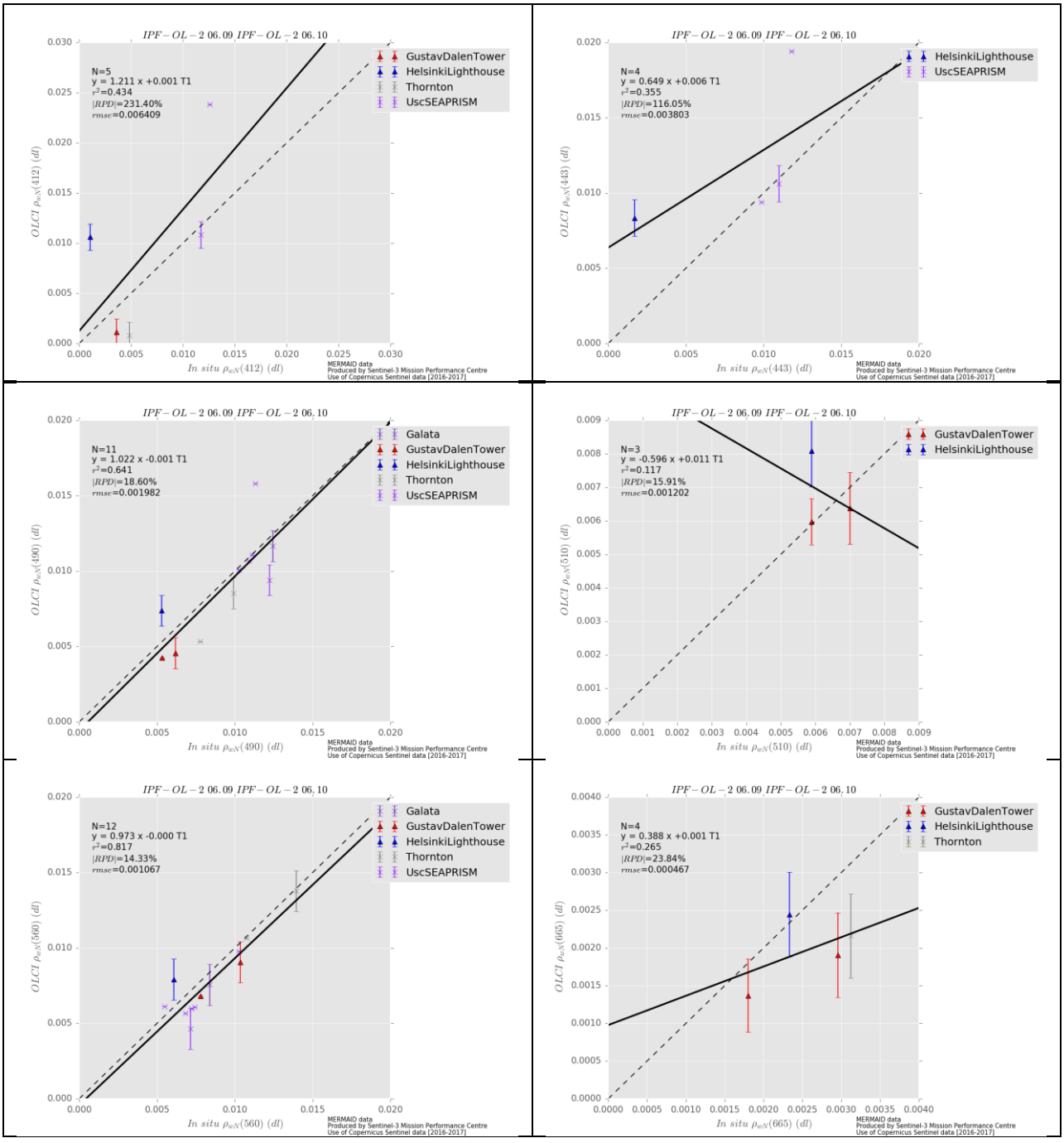

Figure 32: Scatter plots of OLCI versus in situ radiometry (FR data)

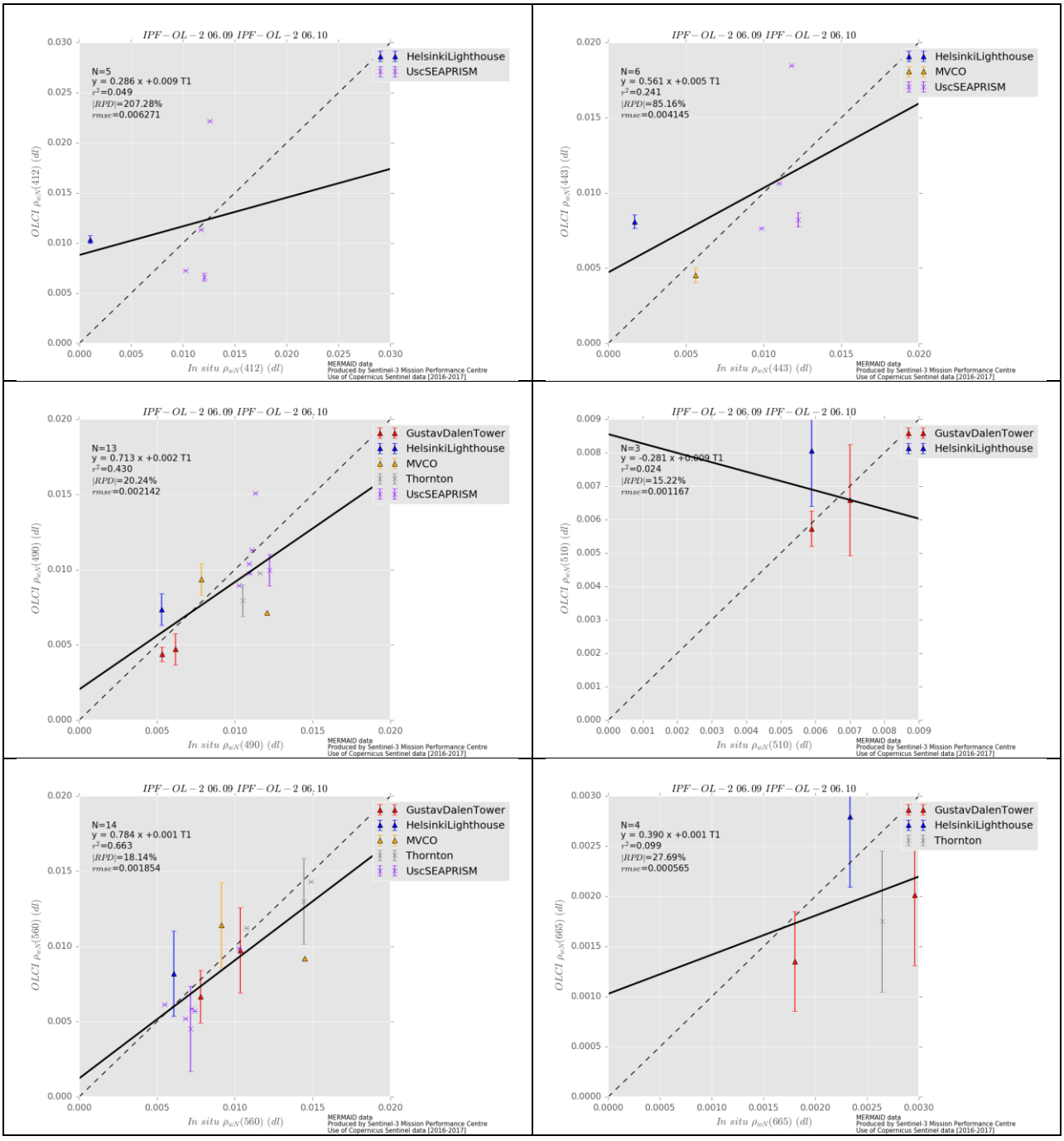

Figure 33: Scatter plots of OLCI versus in situ radiometry (RR data)

Table 2: FR statistics over December 2016-March 2017 reporting period

lambda	N	RPD	|RPD|	MAD	RMSE	slope	int.	r2
412	25	70,55%	77,47%	0,0055	0,0071	0,9486	0,0061	0,6787
443	25	43,34%	44,27%	0,0045	0,0056	1,1251	0,0028	0,9037
490	24	28,53%	28,53%	0,0048	0,0059	1,1634	0,0016	0,9611
510	2	31,69%	31,69%	0,0091	0,0093	2,0459	-0,0207	1,0000
560	17	15,44%	16,95%	0,0037	0,0052	1,1350	0,0003	0,9655
665	25	10,56%	34,24%	0,0010	0,0032	1,3661	-0,0013	0,9236

Table 3: FR statistics over February 2017-April 2017 reporting period

lambda	N	RPD	|RPD|	MAD	RMSE	slope	int.	r2
412	60	88.15%	93.77%	0.0052	0.0066	1.0404	0.0048	0.6176
443	60	46.70%	50.43%	0.0038	0.0049	1.1195	0.0026	0.8046
490	59	31.38%	32.56%	0.0039	0.0046	1.1397	0.0019	0.9263
510	19	27.06%	27.06%	0.0050	0.0055	1.1474	0.0021	0.9486
560	53	13.42%	16.58%	0.0024	0.0035	1.1281	0.0001	0.9379
665	51	1.02%	29.79%	0.0000	0.0012	1.0202	-0.0001	0.7892

Table 4 FR statistics over April 2017-June 2017 reporting period

lambda	N	RPD	|RPD|	MAD	RMSE	slope	intercept	r2
400	2	17.9%	17.9%	0.0088	0.0100	-2.3992	0.1784	1.0000
412	15	66.3%	66.3%	0.0055	0.0062	1.0618	0.0046	0.9611
443	15	36.7%	37.0%	0.0037	0.0044	1.1107	0.0023	0.9454
490	20	32.1%	32.3%	0.0038	0.0044	1.0153	0.0036	0.8224
510	10	35.9%	35.9%	0.0045	0.0048	0.8626	0.0064	0.7505
560	21	17.0%	21.9%	0.0020	0.0034	1.0925	0.0006	0.9205

Table 5: FR statistics over May 1st to July 10th reporting period

lambda	N	RPD	|RPD|	MAD	RMSE	slope	intercept	r2
412	35	30.5%	38.2%	0.0025	0.0060	0.9699	0.0033	0.9364
443	43	25.2%	32.9%	0.0023	0.0061	1.0444	0.0012	0.9546
490	52	15.2%	22.2%	0.0020	0.0055	1.0462	0.0007	0.9756
510	21	24.1%	24.9%	0.0026	0.0039	1.1577	0.0004	0.9946
560	52	2.4%	11.1%	0.0004	0.0045	1.0196	-0.0002	0.9701
665	32	-6.9%	17.7%	-0.0002	0.0023	0.9830	-0.0001	0.8423

Table 6: FR statistics over the current reporting period (July 11th to August 23rd)

lambda	N	RPD	|RPD|	MAD	RMSE	slope	intercept	r2
412	19	18.0%	32.2%	0.0008	0.0066	1.0075	0.0006	0.9346
443	24	10.2%	24.1%	0.0012	0.0072	1.0752	-0.0012	0.9524
490	32	8.0%	18.8%	0.0012	0.0062	1.0504	-0.0005	0.9743
510	10	17.6%	19.3%	0.0011	0.0014	0.9560	0.0014	0.6316
560	32	-1.0%	13.0%	-0.0002	0.0055	1.0179	-0.0008	0.9618
665	22	-10.8%	18.4%	-0.0004	0.0027	0.9028	0.0003	0.7552

Table 7: FR Statistics over the current reporting period (July 1sh to September 7th)

lambda	N	RPD	|RPD|	MAD	RMSE	slope	intercept	r2
412	6	81.5%	95.7%	0.0017	0.0064	0.6848	0.0063	0.7589
443	7	31.6%	49.7%	0.0003	0.0041	0.8661	0.0026	0.9401
490	11	5.8%	20.1%	0.0003	0.0022	0.9909	0.0004	0.9818
510	3	13.0%	20.2%	0.0009	0.0015	1.1289	0.0000	0.1477
560	11	-4.5%	12.9%	-0.0009	0.0021	0.9270	0.0004	0.9784
665	7	-22.5%	22.5%	-0.0008	0.0009	1.0191	-0.0009	0.9618

Figure 34 below shows illustrate the lack of both is situ and OLCI data on the current reporting period..

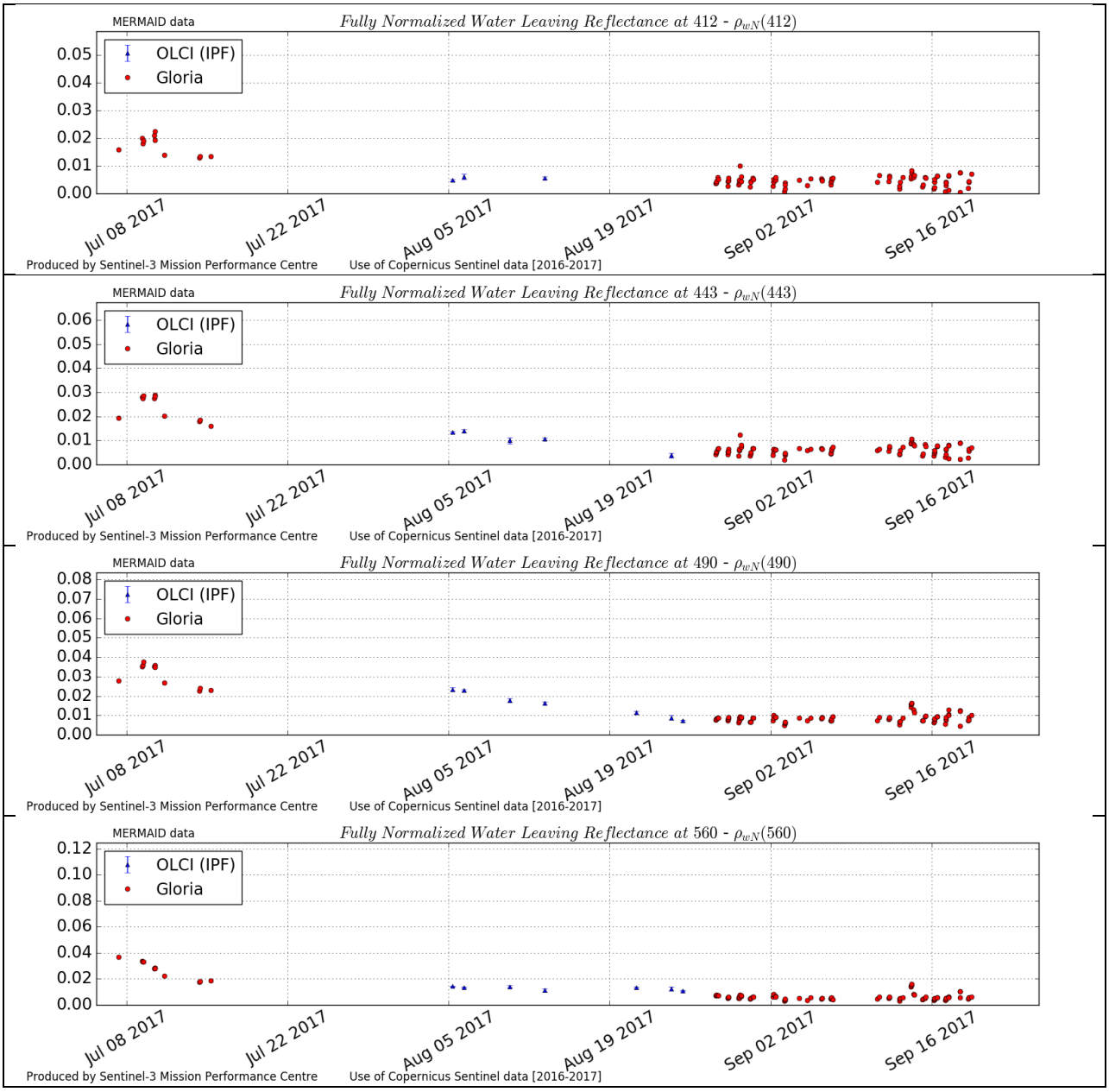

Figure 34: OLCI and AERONET-OC radiometric time on Gloria station.

4.3 [OLCI-L2WLR-CV530] Validation of Aerosol Product

There has been no update on Aerosol Products validation quantitative assessment during the cycle. Last figures (cycle 18) are considered valid.

Qualitative assessment by product inspection showed no detectable performance evolution.

4.4 [OLCI-L2WLR-CV-380] Development of calibration, product and science algorithms

4.4.1 Smile Correction at 681.25 nm (Oa10)

Highlight

An interesting study has been conducted by Spectral Earth, the Spectral Calibration ESL, regarding the impact of OLCI spectral misregistration (in-FOV variation of spectral response functions) on water leaving reflectance around the chlorophyll fluorescence peak at 682 nm.

The study concludes that the full smile correction should be applied to that channel the same way as to others despite the strong non-linear behaviour of the fluorescence signal as it is compensated (at channel Oa10 position) by chlorophyll re-absorption, restoring a quasi-linear behaviour. This brings the smile impact on the water leaving reflectance at 681nm from 4 to less than 1%.

The complete study is reported below.

Investigation Report

We investigate the effect/impact of the non-execution of the smile correction in band 10 (681.25) over ocean, and whether a smile correction could be performed.

Background:

Due to the measurement principle of OLCI, the central wavelengths of all bands vary over the field of view and between the camera interfaces. The absolute spread is in the order of 1.3 nm. This is illustrated in Figure 35, showing the relative spectral response functions of OLCI's bands and their spread.

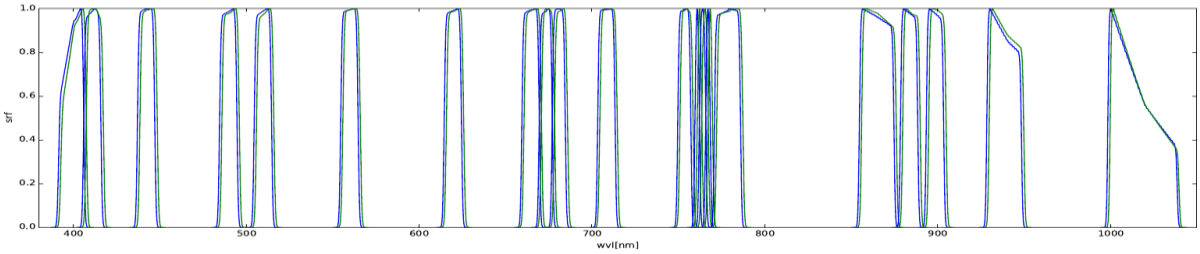

Figure 35: The two extremes of the spectral response function of OLCI A bands

Since the spectral shifts are relatively small, their effect can be easily corrected, if the TOA reflectance behaves linear with respect to wavelength. Currently in the ground segment the correction is implemented as:

$$\rho_{corr}\left(\lambda_0\right) = \rho_{meas}\left(\lambda_{pixel}\right) + \frac{\partial \rho}{\partial \lambda} \cdot \left(\lambda_0 - \lambda_{pixel}\right),$$

approximating the spectral sensitivity:

$$\frac{\partial \rho}{\partial \lambda} \approx \left[\frac{\rho_{meas}\left(\lambda_{2,pixel}\right) - \rho_{meas}\left(\lambda_{1,pixel}\right)}{\left(\lambda_{2,pixel} - \lambda_{1,pixel}\right)} \right]$$

Where ρ_{meas} and ρ_{cor} correspond to a Rayleigh corrected reflectance, the impact of smile on Rayleigh reflectance being accounted for separately.

The index (1 or 2) points to the particularly used neighbor bands (see table 1). The correction is not performed for all bands, as indicated in Table 8. In particular the bands placed at atmospheric absorption bands (Oa13, Oa14 and Oa15 at around the O2 absorption at 760nm, Oa19 and Oa20 in the H2O absorption) are not corrected, since the linear assumption does not hold. Additionally to the absorption bands, band Oa10 is not corrected over ocean. The rationale behind is the chlorophyll fluorescence emission at around 682 nm, which presumably creates nonlinear spectral features similar (but opposite sign) to gaseous absorption.

Table 8: Smile correction configuration of OLCI

	Water			Land			
Band	reflectance correction switch	Lower band	Upper band	reflectance correction switch	Lower band	Upper band	Reference Central wavelength (nm)
O1	1	O1	O2	1	O1	O2	400
O2	1	O1	O3	1	O1	O3	412.5
O3	1	O2	O4	1	O2	O4	442.5
O4	1	O3	O5	1	O3	O5	490
O5	1	O4	O6	1	O4	O6	510
O6	1	O5	O7	1	O5	O7	560
O7	1	O6	O8	1	O6	O8	620
O8	1	O7	O9	1	O7	O9	665
O9	1	O8	**O9**	1	O8	O10	673.75
O10	0	**N/A**	**N/A**	1	O9	O11	681.25
O11	1	**O11**	O12	1	O10	O12	708.75
O12	1	O11	**O12**	1	O11	**O12**	753.75
O13	0	**N/A**	**N/A**	0	**N/A**	**N/A**	761.25
O14	0	**N/A**	**N/A**	0	**N/A**	**N/A**	764.375
O15	0	**N/A**	**N/A**	0	**N/A**	**N/A**	767.5
O16	1	**O16**	O17	1	**O16**	O17	778.75
O17	1	O16	O18	1	O16	O18	865
O18	1	O17	**O18**	1	O17	**O18**	885
O19	0	**N/A**	**N/A**	0	**N/A**	**N/A**	900
O20	0	**N/A**	**N/A**	0	**N/A**	**N/A**	940
O21	1	**O18**	**O21**	1	**O18**	**O21**	1020

Analysis

To investigate the effect of fluorescence on top of atmosphere reflectance, we performed radiative transfer calculations, for a large set of different atmospheric and oceanic states. In particular the inherent optical properties of the water body were varied in a wide range. The simulations were

performed with a spectrally high resolution. This allows the subsequent convolution with any relative spectral response of OLCI. The following figures (Figure 36) show some examples, illustrating the effect of fluorescence and the position of OLCI's bands (the quantities are *above water leaving reflectance*, simplifying the recognition of fluorescence effects). One remarkable feature is that the fluorescence peak is not situated at 682 nm but shifted towards longer wavelengths. The red shift is the result of the interaction of chlorophyll emission and absorption (see Figure 37).

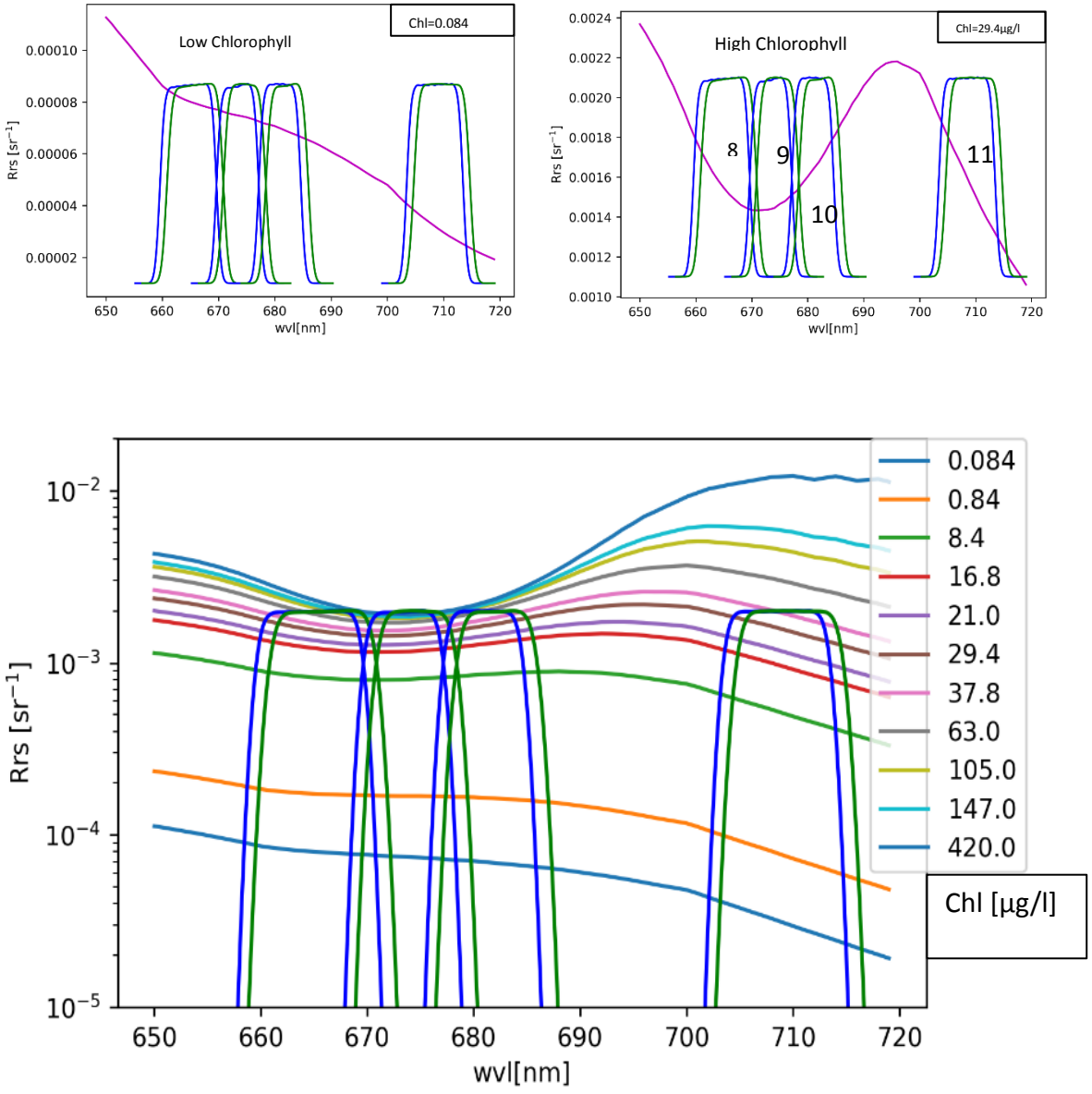

Figure 36: Simulated water leaving radiances for different amounts of Chlorophyll A. Overlaid are the relative spectral response function (and their spread)

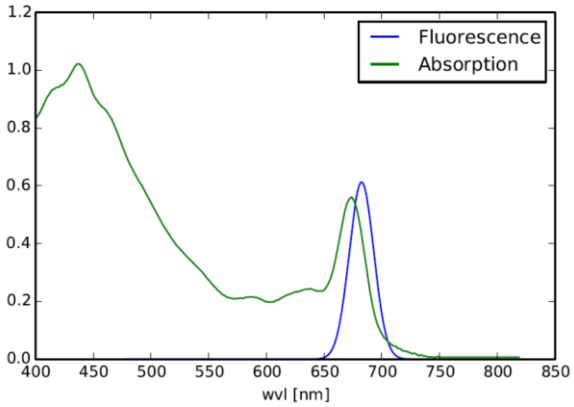

Figure 37: Chlorophyll A absorption and emission (in arb. units)

Afterwards, we quantified the effect of the spectral shift on the water leaving reflectance by convolving the high resolution spectra with the respective response functions. Figure 38 is showing the relative differences arising from the spectral spread for a large range of chlorophyll amounts.

$$\%\Delta Rrs = \frac{1}{2}\frac{Rrs(\lambda_{max}) - Rrs(\lambda_{min})}{Rrs(\lambda_{max}) + Rrs(\lambda_{min})} * 100$$

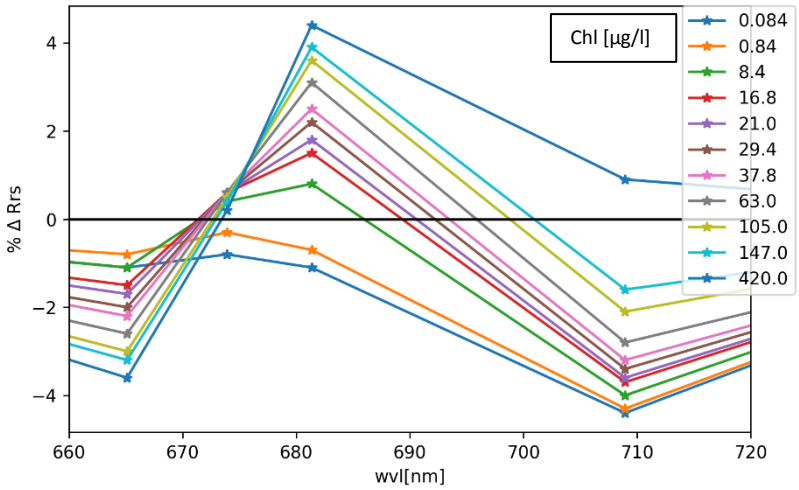

Figure 38: Effect of spectral shift on water leaving reflectance. The dots are the nominal positions of the OLCI Bands 8,9,10 and 11

It turns out that the shift introduced differences of up to 4% in water leaving reflectance. Note, that the differences are smaller at TOA, since the atmospheric path radiance is mainly a constant (or spectrally slowly varying) offset. However for ocean color remote sensing the water leaving reflectance is the relevant quantity. (The influence of residual water vapor absorption around 710 nm has been neglected herein.)

However, looking at the spectral slopes in Figure 36, it turns out, that band Oa10 is **not located in an extraordinary spectrally nonlinear part.** In other words: although band 10 was placed at 681 nm to be sensitive to fluorescence emission, it is not at the most sensitive place. Probably the red shift effect due to chlorophyll re-absorption was underestimated. The good point is that consequently Oa10 can be corrected for the spectral shift as all the other non-absorbing bands. This has been tested, using the bands Oa9 and Oa10 to approximate the spectral differential in eq. 1. The results (again quantified in relative differences of water leaving reflectance) of the linear correction of the spectral spread is shown in Figure 39. Eventually, the effect of the spectral slope is reduced by the linear correction from up to 5% down to below 1%. Band Oa10 does not show any specialties.

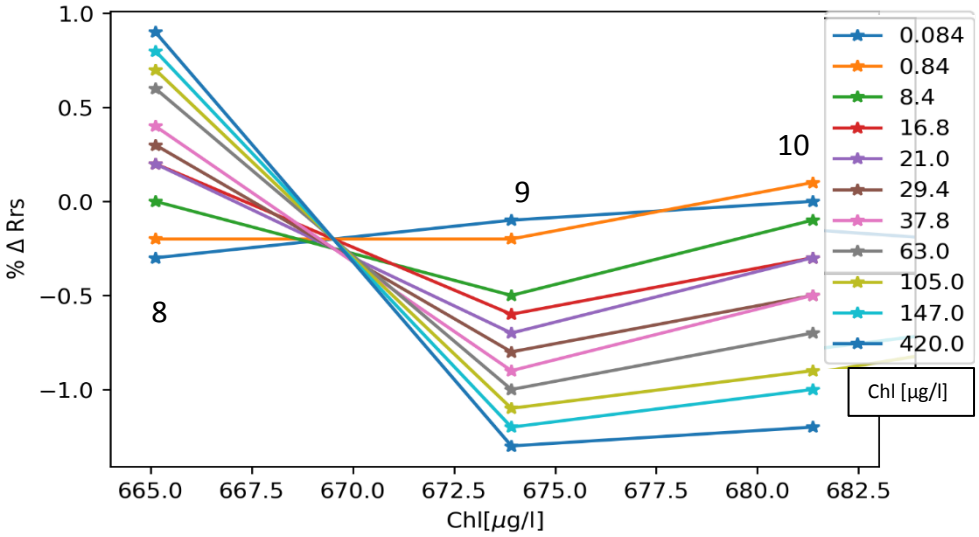

Figure 39: Residual effect of spectral shift on water leaving reflectance after shift correction. The dots are the nominal positions of the OLCI Bands 8,9 and 10.

Conclusion

Due to a non-ideal positioning of band Oa10 with respect to fluorescence, it can be corrected like the other bands. We recommend this configuration update.

4.4.2 Validity of the ANNOT_MIXR1 flag

Analysis

Analysis of an OLCI L2 image has provided interest on the validity of the MIXR1 flag. This flag is raised in the atmospheric correction process as soon as the atmospheric signal in the near-infrared is outside the scope of the radiative transfer look-up-tables used in the retrieval. This is illustrated on a scene over the South Indian Ocean (SIO).

MIXR1 is raised if either the signal is too low because of very small aerosol content (Figure 40), or the signal is too high because of an excess of brightness possibly due to small undetected clouds, small islands or reflecting boats (Figure 41). We also notice the strong effect of thick cirrus shadows which is not dealt with by this flag.

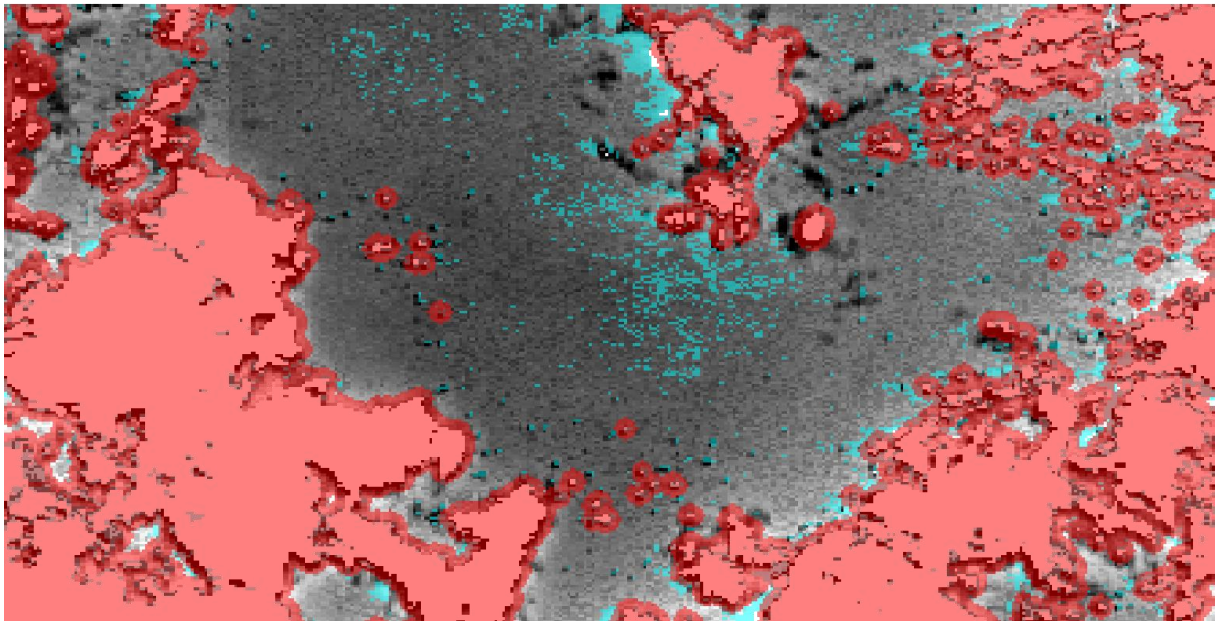

Figure 40 : Oa01 water-leaving reflectance, clouds+cloud ambiguous+cloud margins in red, MIXR1 in blue. MIXR1 is raised because of small AOT in the absence of clouds.

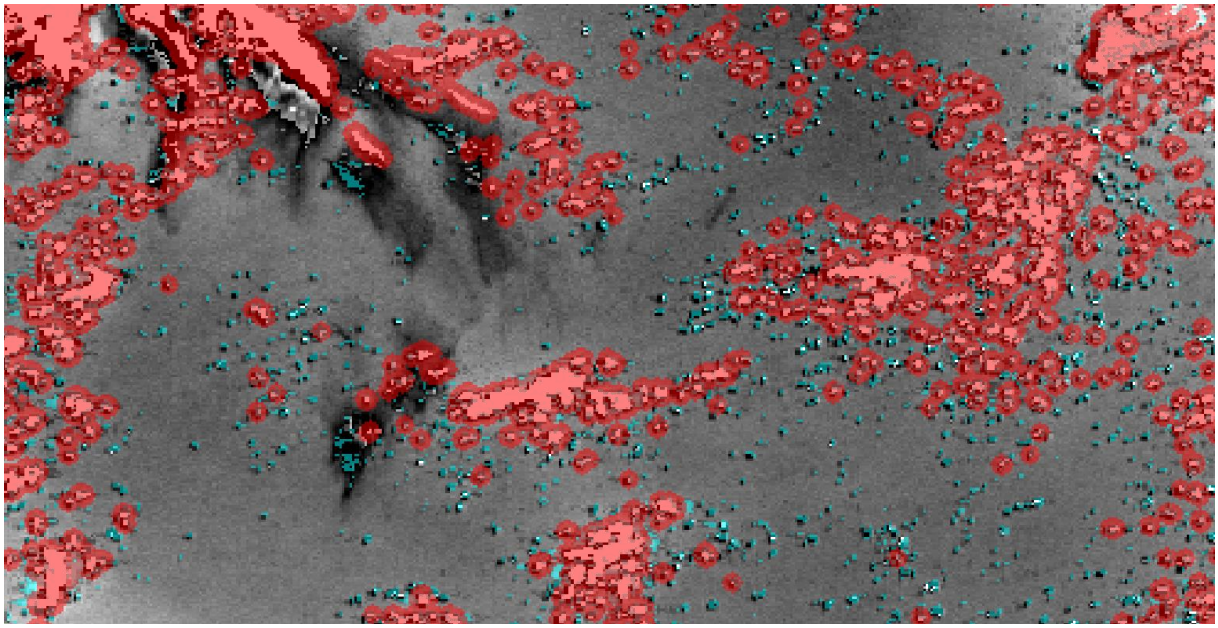

Figure 41 : Oa01 water-leaving reflectance, clouds+cloud ambiguous+cloud margins in red, MIXR1 in blue. MIXR1 is raised because of undetected small clouds.

A statistical analysis of this scene allows to assess the occurrence of raised MIXR1 flags as a function of aerosol optical thickness at 865 nm. This is illustrated in Figure 42.

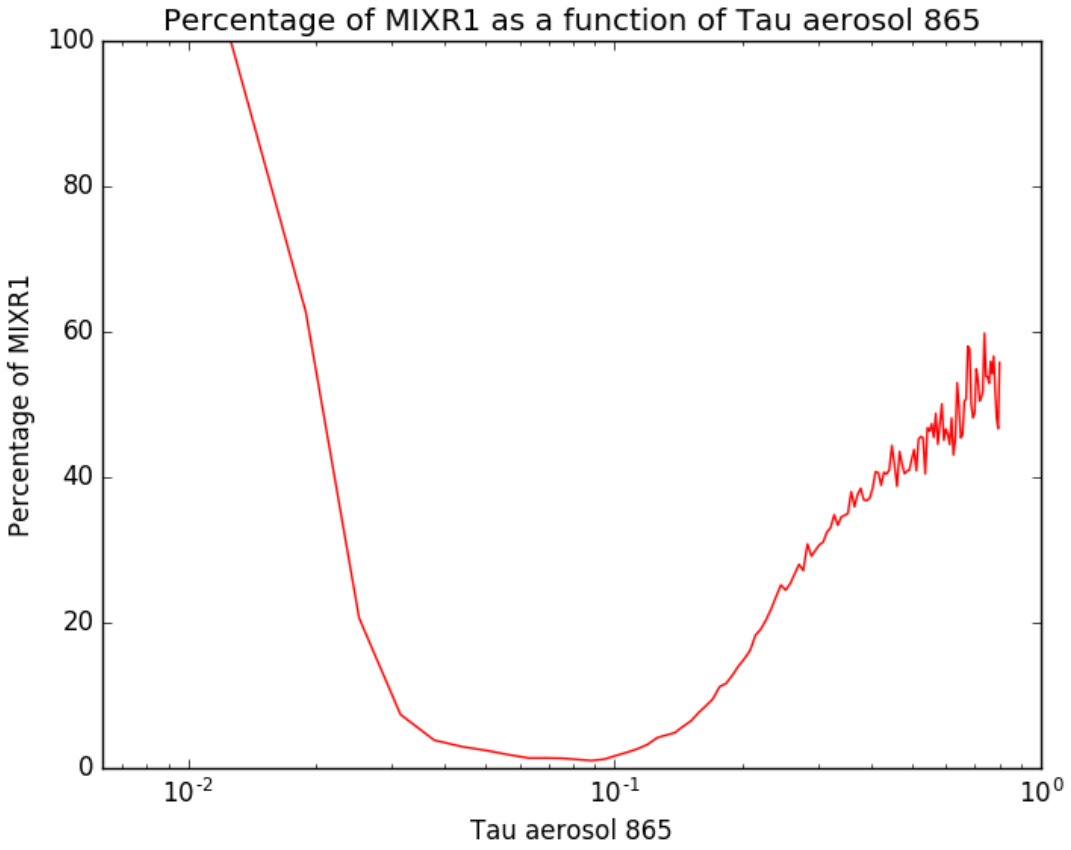

Figure 42 : Frequency of occurrence of raised MIXR1 flags as a function of aerosol optical thickness at 865 nm.

At low aerosol optical thickness MIXR1 is raised because the atmospheric signal is small, then the Angström exponent is also difficult to assess and more uncertain. However, at such low AOTs the impact on the atmospheric signal propagated in the visible is weak so that the final impact on the water-leaving reflectance is small.

At AOTs higher than about 0.1 effects of small clouds or other undetected bright objects is increasing with AOT.

MIXR1 can therefore be used to track down small bright objects that have not been detected in the preprocessing steps. The risk of false alarms increases at low AOTs from a threshold of about 0.05. From such low AOT the effect on atmospheric correction is small and flags out many useable pixels in cloud-free aerosol-free zones as seen in Figure 43.

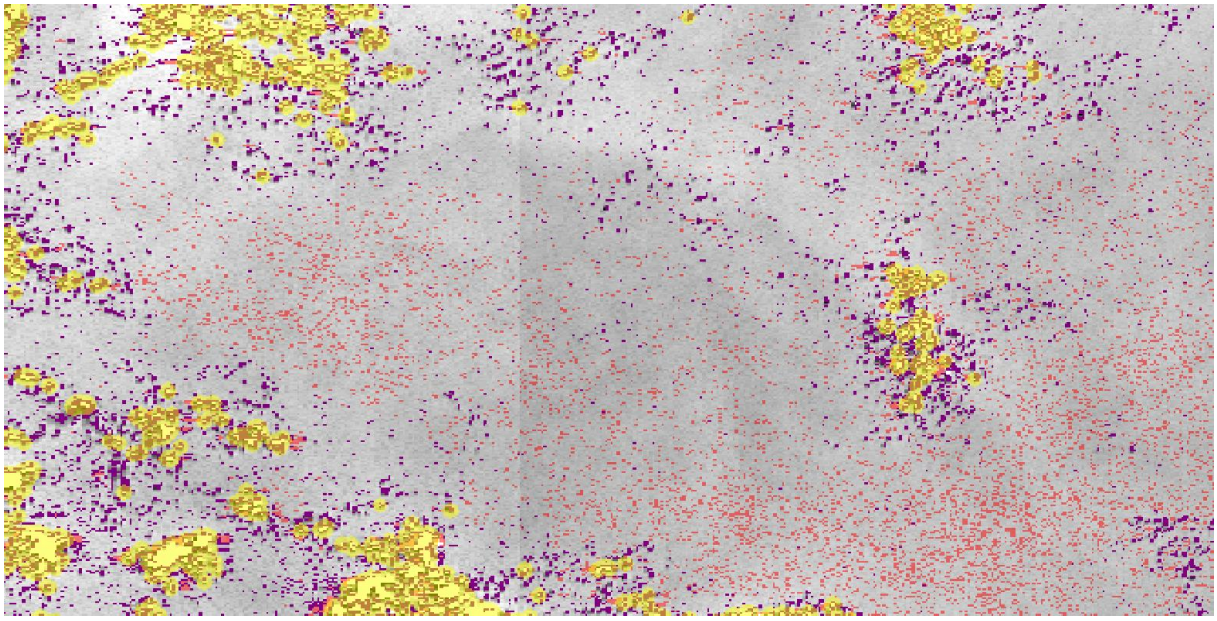

Figure 43 : Oa01 water-leaving reflectance, clouds+cloud ambiguous+cloud margins in yellow, MIXR1 combined to AOT<0.05 in red, MIXR1 combined to AOT>0.05 in violet.

Conclusion

For this reason we recommend to redefine MIXR1 as raised only when AOT>0.05.

5 Level 2 SYN products validation

5.1 [SYN-L2-CV-100]

There has been no new result during the cycle. Last figures (cycle 21) are considered valid

6 Events

Two OLCI Radiometric Calibration Sequences have been acquired during Cycle 022:

- S01 sequence (diffuser 1) on 08/09/2017 17:34 to 17:36 (absolute orbit 8127)
- S01 sequence (diffuser 1) on 22/09/2017 01:24 to 01:25 (absolute orbit 8317)

7 Appendix A

Other reports related to the Optical mission are:

- S3-A SLSTR Cyclic Performance Report, Cycle No. 022 (ref. S3MPC.RAL.PR.02-022)

All Cyclic Performance Reports are available on MPC pages in Sentinel Online website, at: https://sentinel.esa.int

End of document